12-6-2017

FiberBlender: A Realistic Computer Model of Nerve Bundles for Simulating and Validating the Acquisition of Diffusion Tensor Imaging

Teddy Salan

FIBERBLENDER:
A REALISTIC COMPUTER MODEL OF NERVE BUNDLES FOR SIMULATING AND VALIDATING THE ACQUISITION OF DIFFUSION TENSOR IMAGING

by

Teddy Salan

A Dissertation

Submitted in Partial Fulfillment of the

Requirements for the Degree of

Doctor of Philosophy

Major: Electrical and Computer Engineering

The University of Memphis

December 2017

DEDICATION

This dissertation is dedicated to all cancer survivors, including my mother, and to the rest of my family for their love and support.

ACKNOWLEDGMENTS

First, I want to convey my deepest gratitude to my major supervisor Dr. Eddie L. Jacobs for his immense support and patience throughout my graduate studies.

I would like to thank all my teachers at the department of Electrical and Computer Engineering, especially Dr. Chrysanthe Preza and Dr. Madhusudhanan Balasubramanian who devoted their precious time to serve on my dissertation committee and give me guidance in my research.

I would like to thank Dr. Wilburn Reddick from St. Jude Children's Research Hospital who also served on my committee and made this research possible.

Lastly, I am forever thankful to my family for their never-ending encouragement.

PREFACE

This research was supported in part by the National Cancer Institute under grant CA090246. Content from Chapter 3 was published in the *Conference Proceeding of the IEEE Engineering in Medicine and Biology Society* (EMBS), and presented at the *39th International Conference of the IEEE Engineering in Medicine and Biology Society*. Content from Chapters 3 and 4 was submitted to *IEEE Transactions on Biomedical Engineering* and is currently under review.

ABSTRACT

Salan, Teddy. PhD. The University of Memphis. December 2017. FiberBlender: A realistic computer model of nerve bundles for simulating and validating the acquisition of diffusion tensor imaging. Major Professor: Dr. Eddie L. Jacobs.

Diffusion Tensor Imaging (DTI) is a powerful medical imaging technique that provides a unique method to investigate the structure and connectivity of neural pathways. DTI is a special magnetic resonance imaging (MRI) modality that combines the principles of magnetic resonance with molecular diffusion to trace the motion of water molecules. In the central nervous system, where nerve fibers are packed in highly-directional bundles, these molecules diffuse along the orientation of the fibers. Hence, characterizing the motion of water with DTI delivers a non-invasive in vivo technique to capture the connectivity of nerves themselves. Despite its promises and successful clinical applications for nearly thirty years, problems with validation and interpretation of measurements still persist. Most validation studies attempt to generate ground-truth data from animal models, phantoms, and computer models. This dissertation proposes a novel validation system, FiberBlender, capable of reproducing three-dimensional fiber structures and simulating the diffusion of water molecules to generate ground-truth synthetic DTI data. In particular FiberBlender contributes to: (i) creating more biologically accurate representations of fiber bundles with the inclusion of myelin and glial cells, (ii) examining the effect of demyelination and gliosis on DTI measurements, (iii) optimizing acquisition sequences, and (iv) evaluating the performance of multi-tensor models for the study of crossing fibers. FiberBlender strays away from the "one size fits all" approach taken by previous studies and uses computer algorithms in conjunction with some limited manual operations to produce brain-like geometries that take into account the random spatial location of axons and correct distributions of axon diameters, myelin to axon radius, and myelin to glia ratio. In this way no two models are the same and the system is

capable of generating structures that can potentially represent any region of the brain and encompass the heterogeneity between human subjects. This feature is essential for optimization as the performance of DTI acquisition sequences may vary among subjects and the type of scanner used. In addition to better accuracy, the system offers a high degree of flexibility as the geometry can be modified to simulate events that cause drastic changes to the fiber structure. Specially, this dissertation looks at demyelination (an extensive loss of myelin volume), gliosis (a proliferation of glial cells), and axon compaction (a condensation of axons due to a loss of total brain volume) to determine their effects on the observed DTI signal. Simulation results confirm that axon compaction and partial remyelination have similar characteristics. Results also show that some standard clinically used acquisition sequences are incapable of capturing the effects of demyelination, gliosis and compaction when performing longitudinal studies. A novel sequence optimization technique based on Shannon entropy and mutual information is proposed to better capture demyelination. Optimized sequences are tested on a number of non-identical models to confirm their validity and can be used to improve the quality of DTI diagnostics. Finally this work looks at crossing fibers for the validation of multi-tensor models in their ability to characterize crossing diffusion profiles. The performance of multi-tensor models from CHARMED, Q-ball and spherical deconvolution that are widely used in both research and clinical settings are evaluated against ground-truth data generated with FiberBlender. The study is performed on a number of different crossing geometries and preliminary results show that the CHARMED model is the most comprehensive approach.

TABLE OF CONTENTS

LIST OF TABLES

LIST OF FIGURES

SELECTED LIST OF ABBREVIATIONS

AD: Axial Diffusivity

ADC: Apparent Diffusion Coefficient

CC: Corpus Callosum

CHARMED: Composite Hindered and Restricted Model of Diffusion

CNS: Central Nervous System

DTI: Diffusion Tensor Imaging

FA: Fractional Anisotropy

GNR: Glia to Neuron Ratio

HARDI: High Angular Resolution Diffusion Imaging

MD: Radial Diffusivity

MI: Mutual Information

MRI: Magnetic Resonance Imaging

MS: Multiple Sclerosis

PGSE: Pulse Gradient Spin Echo

RD: Radial Diffusivity

SD: Spherical Deconvolution

SNR: Signal to Noise Ratio

TE: Echo Time

WM: White Matter

I. INTRODUCTION

1.1 Overview

Since its inception, magnetic resonance imaging (MRI) revolutionized medicine by enabling a non-invasive in vivo examination of the human body that did not require the harmful use of ionizing radiation such as X-ray and tomography. Conventional MRI exploits the property of nuclear magnetic resonance (NMR) which stipulates that under a strong magnetic field, atomic nuclei can absorb and emit radio frequency (RF) signals. While any nucleus could potentially be used, MRI targets hydrogen as it is the most abundant in the body and forms water molecules. Diffusion tensor imaging (DTI) is a special MRI technique that combines this property with the principles of molecular diffusion to obtain magnetic resonance signals that are sensitive to the movement of water molecules. DTI's advent was particularly useful for examining the brain where the natural random motion of water molecules is constrained by nerve axons, glial cells, and macromolecules such that the net flow of water follows the direction of nerves. In other words, DTI uses the diffusing molecules as probes to obtain microscopic details about the structure and orientation of the fibers themselves.

In the last 25 years, the medical community has been primarily interested in DTI in one of two, yet not necessarily distinct ways. The most innovative application is certainly that of fiber tracking which enables the visualization and mapping of the entire neural connectivity in the human brain [1, 2]. This led to numerous ambitious projects such as the Human Connectome Project that aim at building network maps with unprecedented detail to understand the functional connectivity of the brain [3]. A more direct clinical application is the use of DTI measurements as biomarkers to examine the integrity of nerve fiber tracts for the study and diagnosis of neurodegenerative conditions that cause abnormalities in the central nervous system (CNS).

DTI's clinical capacity has been proven for the categorization of ischemic strokes, tumors, Alzheimer's disease, Multiple sclerosis (MS), traumatic brain injury, and chemotherapy induced neurotoxicity [4-7].

1.2 Problem Definition

Validation in diffusion tensor imaging (DTI) is the problem of establishing an agreement between scanned measurements and the true anatomical properties of the tissue under investigation. Despite its potential some technical and hardware limitations affect DTI data acquisition. The most apparent problem lies with a discrepancy in scale between the observed signal on the scale of millimeters, and the microscopic tissue properties being measured, causing uncertainty in measurements [8]. In other words, DTI properties obtained from a single millimetric voxel are statistical parameters that result from the integration of the combined diffusions at the microscopic scale. This assumes homogeneity of molecular displacements and fiber orientation within a voxel. For this reason the extent to which DTI reveals the true anatomical properties remains the subject of intensive research. The main questions driving DTI validation studies are: How do aberrations in tissue geometry affect the measured signal? And what are the exact physiological events that cause certain measurements?

1.3 Current State of Scholarship

The gold-standard method for validation is to compare DTI measurements with histological evidence from microscopy [9, 10]. Electron microscope images as illustrated in Fig. 1.1 can reveal microstructural details of a fiber bundle with a high degree of accuracy. The axons depicted show a clear sign of myelination with multiple layers of myelin covering them and glial cells in between. However, this approach is not always applicable if DTI is to be used as a

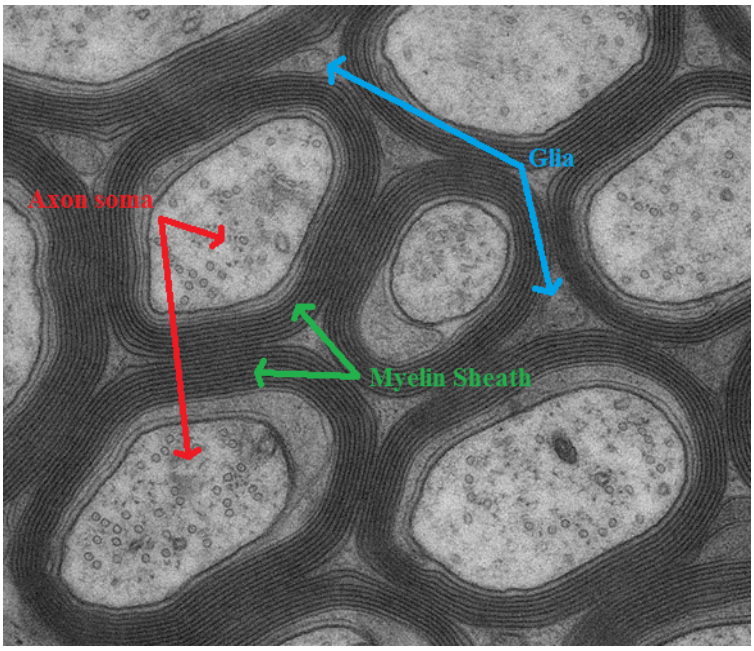

Fig. 1.1: Electron microscope cross-section image of nerve fibers. A myelin sheath wraps around the axon body in several layers with glial cells located between the axons (Credit K. A. Nave / Max Planck Institute for Experimental Medicine [16]).

biomarker for the real-time progression of brain damage and diseases in living patients. Ongoing advances towards intravital microscopy are making it possible to image beyond superficial tissues [11, 12], but they remain far from becoming practical to the human deep brain without surgical procedures. Additional problems lie with the difficulty to reproduce three-dimensional morphology of fibers from two-dimensional slices [13].

Another validation method is *modeling* the fiber tracks of the brain to synthetically produce ground-truth data. These techniques range from ex vivo measurements using post-mortem animal models and physical phantoms, to analytical models and computer simulations. Given the large variety of validation techniques and solutions that are offered, the main issues that have not been addressed in previous research are summarized as follows:

- Models often rely on simplistic representations of axonal geometries that do not account for complex configurations as seen in Fig. 1.1, and therefore cannot adequately represent the *tortuosity* and unpredictable nature of diffusion [14].
- Few studies have considered the presence of a myelin sheath around the axons and to the author's best knowledge, no adequate attempt to model glial cells and their contribution to water diffusion has been published.
- Few studies take into account the presence of water in different compartments (i.e. intra-axonal, myelin, and extra-axonal water).
- No existing methods have attempted to model the *plasticity* of the fiber structure by simulating conditions that cause drastic changes to the geometry (i.e. demyelination, gliosis, and axon compaction) and characterize their effect on the DTI signal [15].
- No robust *optimization* method has been proposed that provides a metric to compare acquisition methods independently of DTI parameters.

This dissertation investigates these crucial aspects in diffusion and proposes a novel modeling and simulation system to accurately represent brain-like fibers, simulate water diffusion, and synthetize ground truth data that can be used to validate and optimize DTI acquisition schemes.

1.4 Approach

The last two decades have seen remarkable advances in the development of powerful 3-D graphics and modeling software. Despite the extensive use of such systems, most notably computer-aided design (CAD) systems in engineering design and simulations, few efforts have taken advantage of this progress for biological modeling in general and nerve representation in

particular. The most widely used tools for scientific simulations include Computational Fluid Dynamics (CFD) systems such as Comsol and Ansys, or systems with Finite Element (FE) methods such as CAD and Abaqus. The work presented herein takes a different approach by using Blender, a free open source software offering a complete 3D creation pipeline, including modeling, simulation, rendering and motion tracking. Although mainly intended for graphic design, computer animation, and gaming its effectiveness for biological modeling has been demonstrated with BioBlender [17], a tool developed for visualizing the surface of moving proteins and understanding the dynamical forces governing molecular interactions.

For the purpose of DTI, the system needs to accomplish two goals: model the fiber geometry and simulate the diffusion of water molecules. Blender delivers many advantages in both areas. As a modeling tool Blender provides more control over the geometry of individual objects and meshes. This allows for more accuracy in representing fibers in non-conventional shapes and configuration, and improves the flexibility of the system as objects can be easily modified and tuned to simulate demyelination, gliosis, or axon compaction. This is essential to modeling both the tortuosity and plasticity of the axon structure. As a simulation tool, a key feature in Blender is its particle system primarily used to simulate phenomena such as fire, dust, clouds, smoke, or in this case liquid particles. Unlike CFD and FE methods Blender relies on Bullet Physics, a powerful physics engine commercially used in games and movies, to calculate particle motion and collision with other interacting objects. Developed in 2006, Bullet uses the Sequential Impulse algorithm [18] to solve constrained rigid body systems and collisions. Extensive comparisons of commonly used physics engines [19, 20] suggested that Bullet Physics displays better accuracy and algorithm convergence in calculating an object's motion, but has lower

predictability, i.e. small changes in the initial conditions yield large variations in the output. This is an acceptable tradeoff in the context of simulating the random diffusion of water molecules.

A scripting option in Blender allows users to programmatically generate objects and simulate events using custom Python scripts. In the presented work, all the simulations have been implemented in Python within the Blender environment while post-processing computations to obtain DTI signals are performed with MATLAB.

1.5 Contribution Statement

The trend in recently published DTI validation methods is to simulate water diffusion to extract synthetic ground-truth data. However the validity of simulations relies on the accuracy of the models in use. Therefore the primary contribution of this work is to provide more realistic representations of fiber bundles that also include myelin, and glial cells. In particular the proposed FiberBlender system strays away from the "one-size-fits-all" approach taken by previous approaches and offers models with a random spatial location of axons to account for the tortuosity of the fiber structure. In addition to better accuracy, spatial randomness allows FiberBlender to generate various models such that no two are the same. This novel feature is essential as most validation techniques are model specific and do no account for the substantial variations among human subjects. Consequently, many published DTI optimization procedures are also model specific and may be sub-optimal or even unfeasible for different subjects or with a different scanner [21].

Furthermore, the produced models are flexible with easily modifiable geometries to account for the plasticity of fiber bundles. This feature is exploited to simulate demyelination and study its effect on the observed DTI signal. Gliosis and axon compaction are additional examples of plasticity examined in this work that have not been addressed in the literature.

The FiberBlender system is also capable of generating models in any desired configuration to potentially mimic different regions of the brain. Specifically this dissertation looks at the problem of crossing fibers and evaluates the performance of non-tensor based diffusion models. The novelty of FiberBlender is its capacity to isolate the particle systems originating from each fiber direction to obtain ground-truth diffusion profiles as a benchmark to compare diffusion models. This step is fundamental for fiber tracking as many simulations show that even the most sophisticated tractography algorithms do not perform consistently well since their accuracy depends on the type of diffusion model used [22].

Finally a novel optimization method is introduced. In the author's assessment of the literature, the problem of optimization in DTI is not well defined since most presented methods are model-specific and it not clear what parameters need to be optimized. In other words, there needs to be a clear metric independent of scanned measurements to quantitatively assess and enhance the quality of scans. This dissertation introduces the notion of optimization based on Shannon entropy and mutual information. While the idea of maximum entropy is commonly used for image registration problems in general as well as for MRI registration, it has not been used in the study of DTI acquisitions.

1.6 Organization

The remainder of this manuscript is organized as follows. Chapter 2 presents a comprehensive chronological synopsis of the emergence of DTI, beginning with the original discoveries on particle diffusion and magnetization up until the modern applications of the technology, and ends with a literature review of the state of the art and its limitations. Chapter 3 begins with a description of the biological properties of axons, myelin and glial cells as requirements for correct modeling strategies, then introduces the FiberBlender simulation system

with all its components, i.e. fiber modeling, particle diffusion, signal acquisition, and baseline experiments. Chapter 4 takes a closer look at the problem of demyelination and its relationship to gliosis and axon compaction to characterize their effect on DTI measurements. The chapter also proposes an optimized DTI acquisition scheme based on mutual information. Chapter 5 provides a comparative study of the most commonly used multi-tensor based diffusion models to evaluate their performance with crossing fibers. The comparison is performed on ground-truth data generated with FiberBlender.

II. EVOLUTION OF DIFFUSION TENSOR IMAGING

In 2003, Paul C. Lauterbur and Sir Peter Mansfield jointly received the Nobel Prize in Physiology or Medicine for their pioneering contributions that led to the application of magnetic resonance in medical imaging. The decision however did not come without controversy from the scientific community for the exclusion of Raymond V. Damadian considered by many to be the true inventor of MRI. Regardless of this verdict, MRI and its extension to DTI are complex multidisciplinary subjects that resulted from decades of research and development in several fields of science and engineering. The purpose of this chapter is to present a historical overview of the emergence of DTI as a way of introducing all the concepts, terms, and equations relevant to later discussions, leading up to the current state of the art in DTI validation and its limitations. The chapter begins with a brief summary of the laws governing the diffusion of molecules, followed by a description of the nuclear magnetic resonance phenomenon due to the interaction of a nucleus with an external magnetic field that led to the invention of MRI. Combining the two ideas, the following sections examine the use of magnetic gradients to produce diffusion weighted magnetic resonance signals and the emergence of DTI as a measure of molecular diffusivity. The final sections shed light on the current limitations with DTI acquisitions and the tensor model, examine the state of the art in current validation techniques, and clarify the need for further improvement.

2.1 On Brownian Motion

The random erratic movement of pollen grains in a fluid was first observed in 1827 by botanist Robert Brown. The driving force behind this phenomenon, later known as Brownian motion, puzzled physicists for many decades until Adolf Fick introduced the notion of diffusion

as one of two fundamental methods of fluid transport [23], the other being advection. Inspired by Fourier's law for heat conduction and Ohm's law for the transport of electric charge, Fick arrived at a simple law that linearly relates the diffusion flux $\boldsymbol{J}$ to the concentration gradient of a substance expressed as

$$\boldsymbol{J} = -D\nabla\boldsymbol{C} \tag{1}$$

where D is the diffusion coefficient and $\boldsymbol{C}$ is the concentration of a substance per unit volume. The negative sign signifies that a solute will diffuse from a region of high concentration to a region of low concentration across a concentration gradient.

Fick's law clarified the macroscopic diffusion process, yet his findings predate the discovery of particles and molecules to explain the individual self-diffusion of water molecules at the atomic level. This description would come later in 1905 when Einstein observed that particles in a solution move erratically due to their thermal kinetic energy [24]. Einstein provided a method to statistically measure the displacement of molecules based on the diffusion coefficient such that the mean-square displacement of particles $< x^2 >$ is given by

$$< x^2 >= nD\Delta t \tag{2}$$

for a diffusion time Δt, and n = 2, 4, or 6 for one, two, or three dimensions respectively. At a body temperature of 37℃, water molecules diffuse at a rate of D = 2.3×10^{-3}mm^2/s. Assuming three dimensional diffusion (n = 6), the average molecular displacement for a period of Δt = 10ms is given by the square root of (2), which yields x = 11.75×10^{-3}mm. However diffusion coefficients measured in biological tissues are generally smaller due to the viscosity of the water in tissue and the interaction of molecules with anatomical structures.

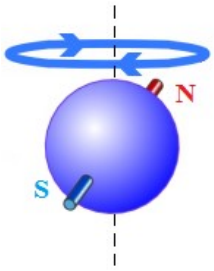

Fig. 2.1: A particle precessing along its main axis.

2.2 Nuclear Magnetic Resonance

In particle physics, atomic and subatomic particles, i.e. protons, electrons, and neutrons, all possess a fundamental property known as spin [25]. Although not entirely accurate, the spin of a particle is often compared to the angular momentum of a precessing gyroscope as demonstrated in Fig. 2.1, keeping in mind that a particle is not actually spinning or rotating. Similar to the precession frequency of a gyroscope that depends on its mass and strength of the gravitational field, the precession frequency of a particle depends on its gyromagnetic constant (γ) and the strength of the magnetic field ($\boldsymbol{B}_0$). This is called the Larmor frequency given by $\omega_0 = \gamma \boldsymbol{B}_0$, and is specific to each particle type. In the context of MRI that deals with hydrogen (^{1}H) contained in water molecules, the nucleus is made of a single particle, a proton, with a Larmor frequency of ~267.53×10^6 rad/s/T. In the literature related to MRI and DTI, the terms nuclei, particles, protons, and spins are often used interchangeably (noting that a spin is not equivalent to a particle but a property of it). To avoid confusion, and to remain consistent with Blender's terminology, from hereinafter this text will refer to them as particles.

When placed in an external magnetic field $\boldsymbol{B}_0$ (Fig. 2.2), a particle ensemble assumes equilibrium state corresponding to the direction of the main magnetic field. The application of a

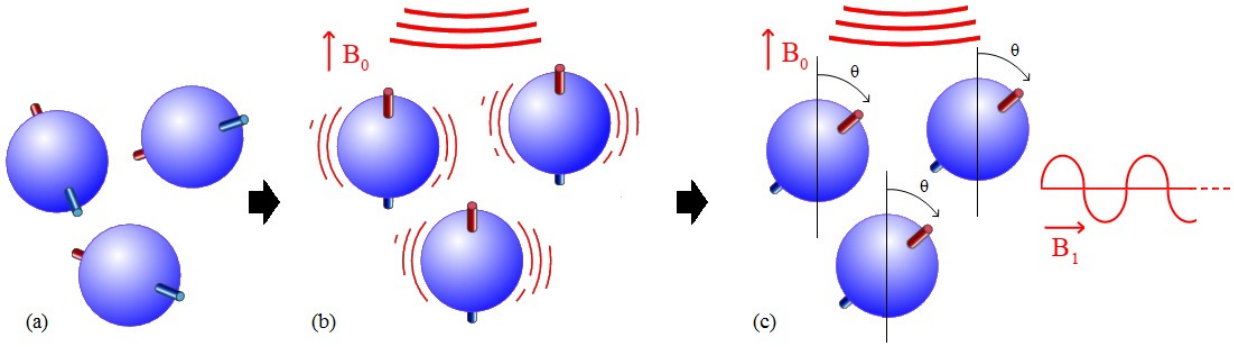

Fig. 2.2: (a) An ensemble of particles. (b) Equilibrium, the particles align along the main magnetic field $\boldsymbol{B}_0$. (c) Excitation, the magnetizations flip in the direction of the RF signal $\boldsymbol{B}_1(t)$.

time dependent RF signal as seen in Fig. 2.2-c irradiates the particles, such that $\boldsymbol{B}_1(t)$ is orthogonal to the main field and modulated at a resonance frequency that corresponds to the hydrogen Larmor precession [27]. This phase called excitation results in a flip of magnetization to a direction perpendicular to $\boldsymbol{B}_0$ – or along $\boldsymbol{B}_1(t)$ – and produces a magnetic flux that can be detected as a small electrical current induced in the receiver coils. This is the signal measured in MRI and is a realization of Faraday's law of induction wherein a changing magnetic field generates an alternating current in a nearby conductor at the Larmor frequency. The flip angle θ between equilibrium and excitation is dependent on the shape and duration of the RF pulse and is given by

$$\theta = \int_0^t \gamma \boldsymbol{B}_1(\tau) d\tau \tag{3}$$

This effect was first observed in 1946 by Felix Bloch [28], then two years later by Nicolaas Bloembergen and his colleagues [29], who recorded transient fluctuations as the system passed through resonance and named it a nuclear induction signal. They also noted that the signal dies after the RF field is stopped as the system of particles returns to equilibrium or the relaxation phase. Bloch introduced the mathematical formulation of this process used to calculate the net

change in magnetization and the intensity of the signal. The Bloch equations as they would become known formed the basis of all MRI studies.

2.3 Bloch Equations

Considering an ensemble of particles with net magnetization vector $\boldsymbol{M} = (M_x, M_y, M_z)$, the effect of the external fields $\boldsymbol{B}_0$ and $\boldsymbol{B}_1(t)$ during excitation is described by

$$\frac{d\boldsymbol{M}}{dt} = \gamma \boldsymbol{M} \times \big(\boldsymbol{B}_0 + \boldsymbol{B}_1(t)\big). \tag{4}$$

In MRI scanners $\boldsymbol{B}_0$ is only applied in the z direction corresponding to the bore of the scanner. This directional frame of reference is used by all researchers and manufacturers. Therefore the strength of the field is given as $\boldsymbol{B}_0 = B_0\hat{z}$ ignoring the xy plane, and (4) is often written as

$$\frac{d\boldsymbol{M}}{dt} = \gamma \boldsymbol{M} \times \boldsymbol{B}(t), \tag{5}$$

where $\boldsymbol{B}(t) = (\boldsymbol{B}_1\hat{x}(t) + \boldsymbol{B}_1\hat{y}(t) + \Delta\boldsymbol{B}\hat{z}(t))$. When the RF pulse is stopped the magnetization vector returns to its equilibrium position along the direction of the main field, or the z direction. This is described by two relaxation mechanisms. The spin-lattice relaxation is the process by which the longitudinal component M_z of the magnetization vector recovers exponentially towards equilibrium and is characterized by T_1, the time required for M_z to reach (1 − 1/e) or 63% its maximum value (Fig. 2.3-a). Conversely, the transverse component M_{xy} decays exponentially to zero and is called the spin-spin relaxation characterized by T_2, the time required for M_{xy} to fall to approximately (1/e) or 37% of its initial value (Fig. 2.3-b). The relaxation terms can now be added to (5) for the complete formulation of the Bloch equation

$$\frac{d\boldsymbol{M}}{dt} = \gamma \boldsymbol{M} \times \boldsymbol{B}(t) - \frac{M_x\hat{x} + M_y\hat{y}}{T_2} - \frac{M_z\hat{z} - M_0}{T_1}. \tag{6}$$

Solutions to (6) for the longitudinal direction z and the transverse plane xy are given as

$$M_z(t) = M_0\left(1 - e^{-t/T_1}\right), \tag{7}$$

$$M_{xy}(t) = M_0 e^{-t/T_2}. \tag{8}$$

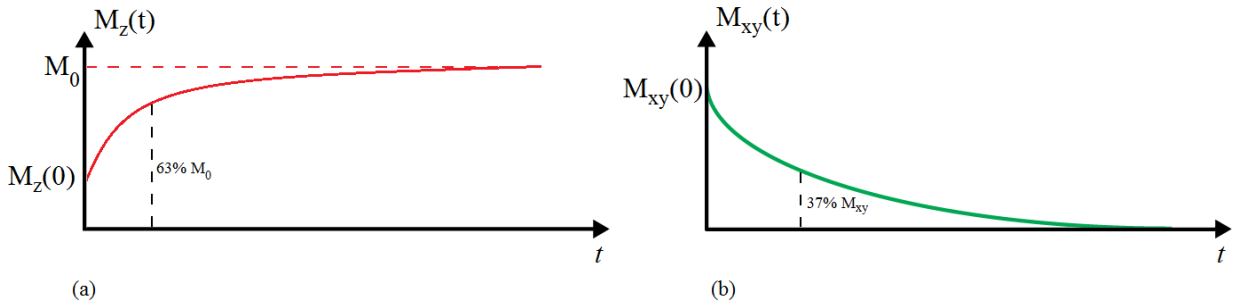

Fig. 2.3: (a) Longitudinal magnetization recovery and (b) transverse magnetization decay.

Time constants T_1 and T_2 are properties of tissues and in general $T_2 \ll T_1$. Table 1 shows longitudinal and transverse relaxation times for different tissue types in the body obtained from the literature measured at 37℃ for 1.5 and 3T [30]. Note that cerebrospinal fluid (CSF) and blood, also present in the brain have much higher relaxation times, for this reason MRI and DTI studies can distinguish them from water contained in white matter (WM) and gray matter (GM).

Table 1. T_1 and T_2 relaxation times at 1.5T and 3T measured at 37°C.

Tissue	$\boldsymbol{T_1}$-3T (ms)	$\boldsymbol{T_2}$-3T (ms)	$\boldsymbol{T_1}$-1.5T (ms)	$\boldsymbol{T_2}$-1.5T (ms)
WM	1084 ± 45	69 ± 3	884 ± 50	72 ± 4
GM	1820 ± 114	99 ± 7	1124 ± 50	95 ± 8
CSF	69 ± 3	69 ± 3	69 ± 3	69 ± 3
Blood	1932 ± 85	275 ± 50	1441 ± 120	290 ± 30
Liver	812 ± 64	42 ± 3	576 ± 30	46 ± 6
Heart	1471 ± 31	47 ± 11	1030 ± 34	40 ± 6

2.4 Pulsed Sequences

Bloch and Bloembergen employed a continuous $\boldsymbol{B}_1(t)$ wave with fixed RF field and could only record small oscillations from the T_2 transverse signal. Meanwhile Erwin Hahn, working simultaneously on NMR was investigating pulsed RF techniques [31, 32].

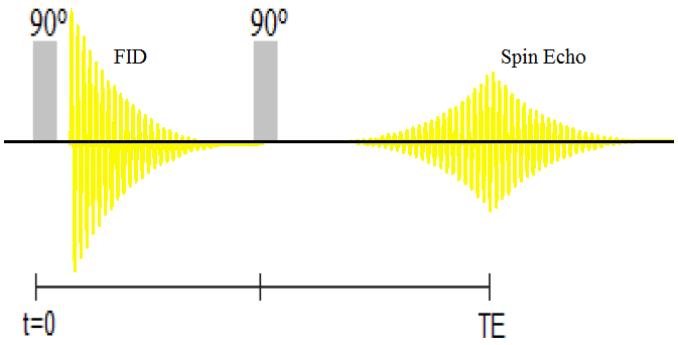

Fig. 2.4: Formation of a spin echo by two RF pulses.

With an RF pulse, Hahn observed a transient sine wave oscillating at Larmor frequency and decaying exponentially, naming it the nuclear induction decay which today is commonly referred to as the free induction decay (FID) signal. With the application of a second consecutive 90° RF pulse at time $t = \tau$ (Fig. 2.4), Hahn also witnessed the formation of a second FID and named it the spin echo formed at echo time (t = TE) such that $\tau = \mathrm{TE}/2$. He noted that the difficulty in measuring the first FID signal was due to a loss of coherence of particle phases from the inherent inhomogeneity of the background magnetic field. Although Hahn first used a 90°-90° pulse pair, most sequences today use a second pulse at 180° (Fig. 2.5-c) as this maximizes the intensity of the spin echo. The second RF pulse inverts the phase accumulated by particles and restores the coherence to form a more measureable echo signal (Fig. 2.5-d). Hahn remarked that the loss of coherence was also due to the diffusivity of particles, thus setting the stage for the development of diffusion MRI.

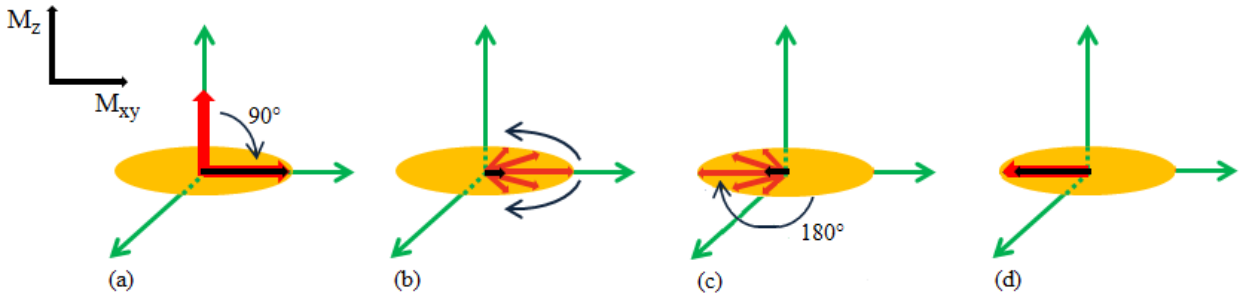

Fig. 2.5: (a) Magnetization flip after the application of a 90° $\boldsymbol{B}_1(t)$ pulse at t = 0. (b) Dephasing after $\boldsymbol{B}_1(t)$ is turned off. (c) Second 180° $\boldsymbol{B}_1(t)$ pulse applied at $t = \tau$ initiates re-phasing. (d) Re-phasing is complete and a measurable spin echo signal is generated at time t = TE.

2.5 Spatial Localization and the First Scanners

The work presented by Bloch, Bloembergen, and Hahn laid the foundation for MRI, and in 1952 Herman Carr produced the first one dimensional MRI image [33]. Yet all the experiments so far were performed on water and other fluids, not on human or animal bodies. This idea would first come 1971 when Raymond Damadian [34] proposed that tumors and normal tissue can be distinguished by their relaxation times with in vivo NMR. However the feasibility of generating 2D pictures from a scan was not determined. Two problems remained unanswered to produce such images. First is the problem of spatial localization in order to receive an NMR signal from a specific region of interest (ROI) in the body, and second is the problem of performing scans in realistic time. In 1973, Paul Lauterbur proposed a revolutionary technique using magnetic gradients to spatially modify the Larmor frequencies of particles, and capture the NMR signal using a Fourier frequency decomposition of the spin echo [35]. Since the Larmor frequency is relative to the strength of the magnetic field, gradients can be used to spatially modify the frequency such that only particles from a particular point in space will emit an NMR signal. While this proved crucial to obtaining spatial specificity it still required hour long scans. In 1975

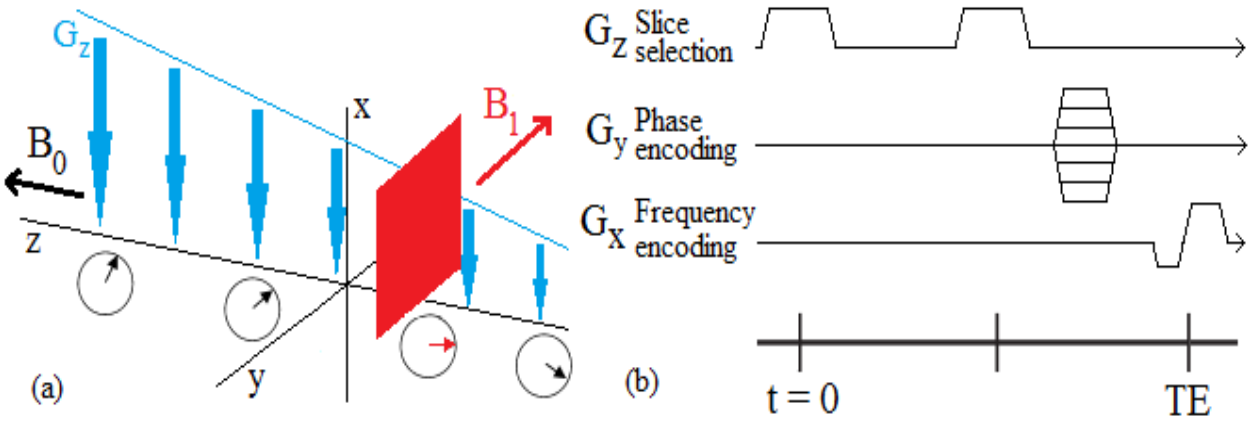

Fig. 2.6: (a) Diagram showing an example of slice selection (red plane) along the z axis (b) Pulse sequence timings of spatially encoding gradients with slice selection pulse G_z, phase encoding pulse G_y and frequency encoding pulse G_x.

Peter Mansfield developed an echo planar echo imaging (EPI) technique to cover a 2D slice with a single FID readout greatly reducing scan times [36].

A demonstration of this procedure is shown in Fig. 2.6-a. A gradient G_z is used simultaneously with the RF pulses to create a spatial variation of Larmor frequencies along the z-axis. Therefore when the RF pulses are applied, only a single slice of particles with corresponding frequency will get magnetized. G_z is called the slice selection pulse. After slice selection (Fig. 2.6-b), two more gradients are used to spatially encode particles in the sample. A phase encoding gradient in the y direction is applied for a range of amplitudes to record the rate of change of particle phases, then at t = TE a gradient in the x direction is applied to frequency-encode the particles. This method allows MRI data to be directly mapped to a spatial frequency domain called k-space with frequency and phase corresponding to the k_x and k_y axes respectively. Image acquisition is therefore reduced to resolving the 2-D inverse Fourier transform of the k-space data.

Peter Mansfield's EPI technique uses phase and frequency pulse trains to rapidly traverse the k-space in a single scan thereby reducing scan times from several hours to a few minutes. In 1977 the first image of vivo human anatomy was performed by Mansfield on his colleague's finger, and in 1980 the Mark 1, the first fully functional and non-experimental MRI scanner, obtained the first clinically useful MRI image of a patient's internal tissues.

2.6 Diffusion Sensitization

Although the application of diffusion MRI would not see the light of day until the 1980's, the initial mechanisms were first introduced by Henry C. Torrey in 1956 [37]. Torrey extended the Bloch equations and introduced a diffusion term such that

$$\frac{d\boldsymbol{M}(r,t)}{dt} = \gamma \boldsymbol{M}(r,t) \times \boldsymbol{B}(r,t) - \frac{M_x\hat{x} + M_y\hat{y}}{T_2} - \frac{M_z\hat{z} - M_0}{T_1} + \nabla \cdot (D\nabla \boldsymbol{M}). \tag{9}$$

In this formulation, the magnetization $\boldsymbol{M}$ and field strength $\boldsymbol{B}$ are functions of both time and r the displacement of a particle and D is the particle diffusion coefficient introduced at the beginning of this chapter. Stejskal and Tanner in 1965 [38] developed a solution for (9) by introducing magnetic gradient pulses, in a similar fashion to spatial encoding gradients, but for the purpose of sensitizing the NMR signal to diffusion and measuring D.

The diffusion weighted Stejskal-Tanner sequence in Fig. 2.7, more commonly known as the pulse gradient spin echo (PGSE), remains one of the most commonly used sequences for routine clinical DTI image and data acquisition. A typical PGSE sequence contains two periods of equal duration T for a total echo time TE = $2T$. Similar to the Hahn sequence, at t = 0, a 90º RF pulse magnetizes the particles, followed by a gradient pulse at an arbitrary time t_1 with strength g and duration δ. The pulse dephases the magnetization of particles along its direction. In the next period, a 180º RF pulse refocuses the spins, and a second gradient pulse of equal strength and

duration but opposite direction rephases the magnetization of the spins. The second gradient is separated from the first by duration Δ.

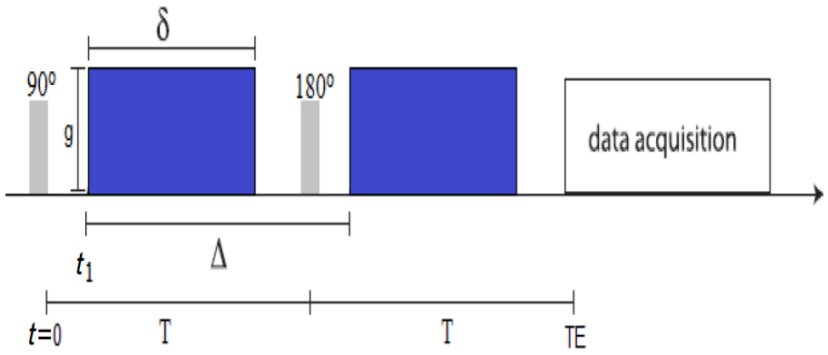

Fig. 2.7: Pulse gradient spin echo (PGSE) sequence with pulse strength g, width δ, and distance between the two pulses Δ.

The original solution to the Bloch equation given in (4) and (5) along the longitudinal direction and transverse plane can be combined as,

$$S_0 = M_0\left(1 - e^{-t/T_1}\right)e^{-t/T_2}, \tag{10}$$

such that S_0 is the NMR signal without diffusion as detailed in previous sections. Factoring in the diffusion sensitizing gradients, Stejskal and Tanner observed an attenuation of that signal. The solution to the Torrey-Bloch equation (9) becomes

$$S = M_0\left(1 - e^{-t/T_1}\right)e^{-t/T_2}e^{-Db}, \tag{11}$$

simplified as

$$S = S_0 e^{-Db}, \tag{12}$$

where D is the diffusion coefficient and b is the degree of sensitization to diffusion given by the gyromagnetic ratio of hydrogen γ, and the characteristics of the gradient pulse g, δ, Δ such that

$$b = \gamma^2 g^2 \delta^2 \left(\Delta - \frac{\delta}{3}\right). \tag{13}$$

To fully understand the effect of diffusion gradients on the signal attenuation, consider the diagram depicted in Fig. 2.7. Since the Larmor frequency of precession is proportional to the strength of the magnetic field, the precession rate in the absence of magnetic gradients is uniform (Fig. 2.8-a). The application of the first gradient dephases the precessions and particles start to precess at different rates depending on their spatial position along the gradient (Fig. 2.8-b). The second pulse rephrases the particles (Fig. 2.8-c). For non-diffusing particles, the phase change induced by both gradient pulses will cancel out and the NMR signal is not affected. However, when a particle moves, there will be a phase difference resulting in an attenuation of the NMR signal proportional to the distance travelled along the direction of the gradient.

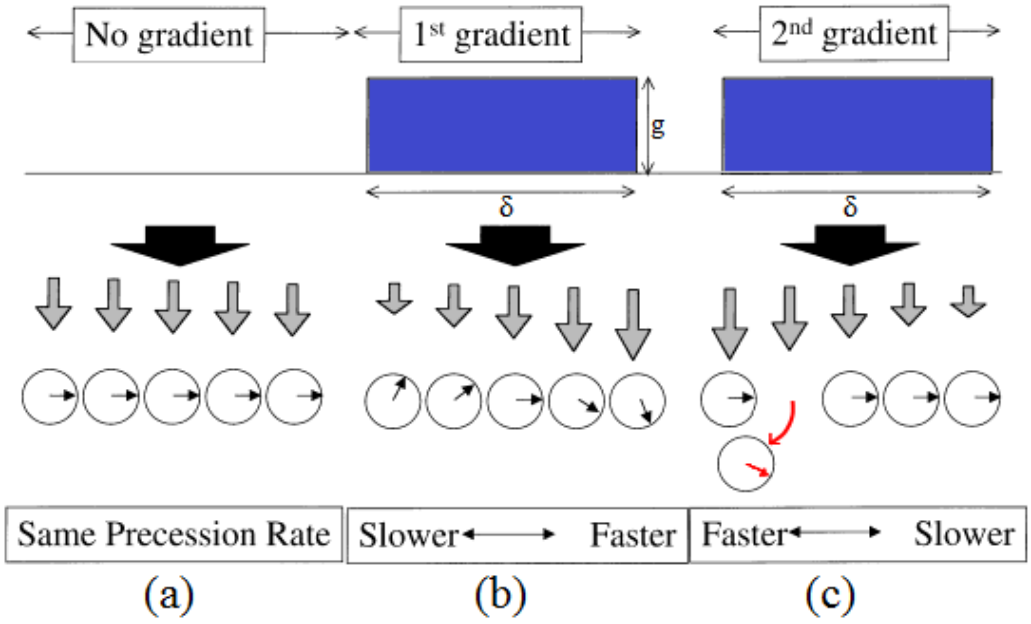

Fig. 2.8: Diagram showing dephasing and rephrasing due to magnetic gradients. (a) With no gradients all particles precess at the same rate given by the uniform field $\boldsymbol{B}_0$. (b) The first gradient dephases the particles by modifying the rate of precession. (c) Particles rephrase if they maintain the same position.

2.7 Diffusion Tensor Imaging

The application of the diffusion gradients to imaging did not attract attention until the mid-1980's when Le Bihan's seminal work incorporated the Stejskal-Tanner sequence to produce the first in vivo diffusion weighted MRI images of the brain [39, 40]. Le Bihan introduced the notion of an apparent diffusion coefficient (ADC or D_{app}), replacing D to indicate that water diffusion in the brain is not free, but is restricted by nerve fibers. ADC can be quantitatively measured from (12) by obtaining both the baseline signal without diffusion gradient (S_0) and signals with gradients applied (S) to solve for

$$D_{app} = -\frac{\ln(S/S_0)}{b}. \tag{14}$$

With this approach, ADC maps can be produced as a measure of diffusivity in each image pixel to create diffusion contrast in MRI images. Potential clinical applications of diffusion MRI were suggested very early, with the most successful application in ischemic strokes [41 - 43], and tumors [44, 45]. Building on Le Bihan's results, in 1994 Basser introduced a diffusion tensor and tensor-based metrics to better describe the diffusivity of particles [46, 47]. Basser's method reformulated the ADC, no longer as a single scalar, but as a 3×3 tensor (Fig 2.9-b) fully describing molecular diffusion in all directions such that

$$S = S_0 e^{-b\, g^{\mathrm{T}} \mathbf{D} g}, \tag{15}$$

with

$$\mathbf{D} = \begin{bmatrix} D_{xx} & D_{xy} & D_{xz} \\ D_{yx} & D_{yy} & D_{yz} \\ D_{zx} & D_{zy} & D_{zz} \end{bmatrix}. \tag{16}$$

Because the tensor has 6 components, a minimum of 6 signals are required from different non-collinear gradients directions g_k (k = 1,…,6; $k \geq 6$) with corresponding signals S_k in addition to

the gradient-free signal S_0 used a reference. The eigenvalue and eigenvector decomposition of the tensor (λ_1, λ_2, and λ_3 in Fig. 2.9) give the amount of diffusion along the principal axes with λ_1 as the main axial diffusivity (AD) and λ_2, λ_3 as the amount of radial diffusivity (RD) while the mean diffusivity (MD) is used as the measure in all directions. Another tensor-derived parameter and perhaps the most widely used is Fractional Anisotropy (FA) calculated as a 0 to 1 scalar describing the degree of anisotropy in a ROI. A value of 0 denotes an isotropic diffusion equal in all directions, in contrast a value of 1 denotes a highly anisotropic diffusion confined to a single direction.

Basser's tensor model further opened the door to new applications for DTI. Interest quickly grew for the study of neurodegenerative disease such Alzheimer's [48, 49], and MS [50 - 52] by recording variations in AD, RD and FA to understand how diseases affect neural tracts. More recently attention turned to studies on chemotherapy [53, 54]. In parallel, DTI based tractography gained momentum and by 1999 the first representations of in vivo tractography successfully reconstructed well-known fiber bundles in the human and animal brain [55 - 57].

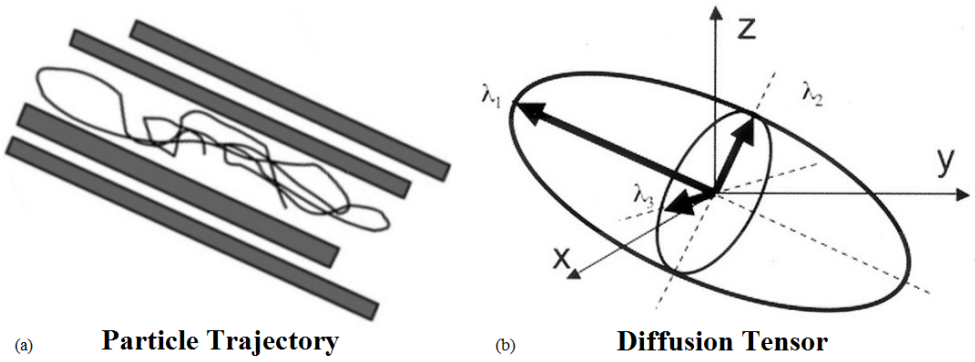

Fig. 2.9: (a) Diagram showing the trajectory of a particle hindered by fibers. (b) The diffusion tensor outlining the particle's main directions of movement with $\lambda_1$as the main axial diffusivity component and λ_2, λ_3 as the radial diffusivity components.

2.8 Problems with DTI and the Need for Validation

Despite the promises of DTI-based studies, concerns regarding the accuracy of measurements developed early [58]. As highlighted in the previous chapter, the main limitation in DTI is the discrepancy between the scale of a voxel and the biological features to be measured. The diffusion tensor is a macroscopic statistical displacement profile of all the combined microscopic diffusions and assumes homogeneity within a voxel. This becomes particularly problematic when considering fibers in multiple orientations (i.e., crossing, kissing, and bending). Resolution limits are due to MRI hardware. The highest clinically feasible diffusion voxel resolutions are about 1.4×1.4×1.4mm, or about 8 times the resolution of conventional MRI [59]. Higher resolutions can be obtained along a specific plane by using non-isotropic voxels (e.g. 0.4×0.4×7mm), but this approach heavily biases the measured diffusivity along the orientation of the voxel [60] and negatively impacts signal to noise ratio (SNR) and spatial specificity, requiring significantly longer acquisition times [58]. Low SNR also biases measurements and over-estimates FA values in tissues [61]. Imaging artifacts from head motion, eddy currents, and inhomogeneity in the magnetic field are additional intrinsic problems to DTI that depend not only on the voxel size but also on the choice of pulse sequence parameters and gradient orientation [39, 62].

In addition, water particles are contained in several tissue compartments with different diffusion profiles, i.e. water within the axon (intra-axonal), in between axons (extra-axonal), and myelin water. It is generally understood that particles in the extra-axonal space undergo a hindered diffusion, and move more freely than in the intra-axonal space under restricted diffusion [63]. However, the contribution of particles in myelin water to the observed DTI signal remains unclear since current processing techniques lack tissue specificity and many models

assume that myelin water has no direct signal contribution because of its low density and short T_2 relaxation time [64].

These obstacles create inconsistencies between DTI-derived measurements and the true anatomical properties of tissues. Nevertheless, DTI is likely to remain a widely used tool in neuroscience as it is currently the only noninvasive method that allows visualization of WM pathways in vivo [58]. For this reason, there has been growing interest in recent years to provide methods that can quantitatively validate DTI acquisition.

2.9 State of the Art in DTI Validation

DTI's unique in vivo and non-invasive quality propelled its success. Conversely, this has also made it difficult to validate measurements. Histological validation normally considered gold-standard is not always applicable for longitudinal studies of the pathological evolution of disease and abnormalities in the CNS. Another direction is modeling brain fibers and simulating DTI to produce ground-truth synthetic data and validate clinical observations. These methods largely fall under four categories: Analytical models, animal models, phantoms, and computer simulations. The last 10 years in particular have witnessed an increasing interest in computer simulation using a Monte-Carlo (MC) process to simulate particle diffusion. The following sections take a deeper look at each of these approaches.

2.9.1 Animal Models

Animal studies account for much of the medical progress in understanding the dynamics of diseases, infections and toxicities. This is no different to DTI and animal experiments began early, usually relying on rat models and non-human primates [65 - 70]. The procedure involves injecting axonal tracers in fiber tracts, typically manganese ion, followed by post-mortem ex vivo data acquisition. Animal models have the clear advantage of using real biological tissues

and early testing was successful. Studies in [66] and [67] demonstrated DTI's precision in identifying the effects of demyelination and ischemia on FA, AD and RD measures, and in 2001 Lin [68, 69] performed the first validation experiments of DTI tractography using animal models confirming accuracy by superimposing DTI images with manganese-enhanced MRI tracts. However animal WM structures, specifically from rat brains, cannot capture the complexity of fiber arrangements that exist in human brains [71], and thus may not be sufficient to evaluate the inherent limitations of diffusion tensor models with respect to tractography and resolve complex fiber configurations. These models also lack the plasticity to tune geometric parameters for a progressive study of demyelination and other structural variations. Furthermore, this method relies on the intravenous injection of tracer and post-mortem acquisitions invalidating DTI's noninvasive and in vivo property.

2.9.2 Phantoms

Phantoms are another example of broadly used models and can be categorized as physical (or hardware) phantoms and software phantoms. Similar to animal models, physical phantoms can provide experimental data through conventional DTI scans, but offer more flexibility in modifying the geometry. Physical phantoms are usually produced as hollow capillaries [72 - 76] or synthetic fibers [77 - 81] with each type presenting different material properties. Hollow capillaries have the advantage of capturing both intra-axonal and extra-axonal diffusions but cannot be used to build complex configurations such as crossing and bending fibers. On the other hand synthetic fibers are more flexible with tunable axon sizes and can be formed with geometries similar to WM bundles, but they are limited to simulating the extra-axonal compartment. In addition neither of the above materials has modeled myelin formation around the axons and cannot represent the properties of biological tissues in terms of compartment

permeability and viscosity. Moreover, manufacturing hardware phantoms with suitable complexity can be very challenging therefore another approach is to use software phantoms. An advantage with software is the ability to test DTI acquisition degradation (e.g. simulate acquisitions at different SNR levels) which is impossible with hardware phantom since the data is acquired by an MR scanner in the first place. Although existing software phantoms are generally very flexible [82 - 85], most of them are not accurate in terms of spatial geometry, WM bundle organization, or acquisition protocol in a unified framework. More recently, the Fiberfox phantom [86] released in 2013 and D-BRAIN phantom [87] released in 2015 tackled some of these problems and are able to provide far more realistic fibers and generate data following standard DTI acquisition protocols. However Fiberfox requires extensive manual operations and expert neuroanatomical knowledge since fiber strands are drawn by a user making it impractical and time-consuming, whereas D-BRAIN requires almost no manual intervention by reconstructing WM structures from DTI data but is susceptible to errors if the input DTI data itself is corrupted during acquisition. Another disadvantage with software based DTI acquisitions is the difficulty to correctly model the underlying mechanisms of water diffusion in neural tissues, specifically with different water compartments.

2.9.3 Analytical Models

Some analytical modeling studies provided insight into intra-axonal and extra-axonal diffusions by using different diffusion coefficient following Gaussian mixture models to predict particle diffusion in each compartment, or by estimating water exchange rate between compartments [88, 89]. However due to the difficulty in representing axons at random locations, analytical models are not widely used and typically rely on simple hexagonal or “honeycomb” organization with uniform axon diameters (Fig 2.10) since analytical expressions for complicated

geometries may not exist. While this is optimal for compactness, the repeating pattern creates periodicity in the displacement of molecules in sharp contrast to the tortuosity of more realistic arrangements. For this reason analytical models can only model parallel axons and cannot be used in studies on crossing fibers and tractography.

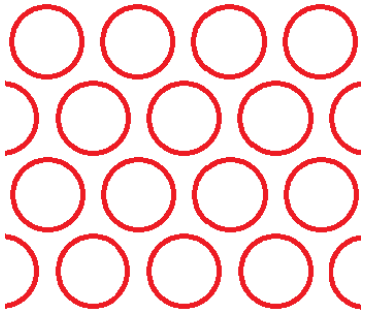

Fig. 2.10: Example of a hexagonal array or honeycomb of axons.

2.9.4 Computer Simulations

Most recently, computer simulations have been the most widely chosen approach to generate synthetic DTI using MC methods to simulate particle diffusivity like the systems described in [64], [71], and [90 - 98]. Similarly to software phantoms these models offer high flexibility; the simulations performed by Yeh [71], Wang [91], and Landman [92] in particular can manipulate their geometries to simulate swelling and axonal damage. Simulations based on MC method also have the potential to remove most of the assumptions regarding particle motion inherently required by software simulations and analytical approaches. Yet the most intrinsic challenge is that they require an adequately large sample size (the number of particles) in order to ensure the stability and reliability of the results that can prove to be demanding in terms of computing power. In 2013 Yeh, Le Bihan, and their collaborators introduced Diffusion Microscopist Simulator (DMS) [71] which offers the most comprehensive system to date. DMS is capable of rendering 3D axonal structures in any combination of crossing, beading, and bending geometries;

generate diffusion data based on standard clinical acquisition protocols using a number of different gradient sequences; and synthetize MR images. Particle diffusion is modeled on MC-based simulations and uses an octree structure to partition the simulation space for better computing efficiency. Still, as with other computer approaches, DMS relies on a simple hexagonal configuration (Fig. 2.10) and cannot produce realistic brain-like WM bundles. Hall and Alexander [96] even proved that models using hexagonal axon arrays can be easily reproduced analytically, questioning the purpose of using computer simulations the first place. Among the computer systems mentioned only a few were able to generate fibers at random locations. However in Fieremans' model [98] all the axons have the same diameter and overall poor compactness. The studies reported by Harkins [64] and Hall [96, 97] were capable of producing non-uniform diameter distribution in addition to randomized locations to create a realistic tortuous simulation space, but they can only generate parallel axons conforming to a single distribution, and only Harkins [64] and Mauconduit [90] include myelinated fibers. Harkins provides the only simulation system that encompasses randomly located and myelinated axons with separate inter-axonal, myelin and extra-axonal water diffusion profiles, as well as water exchange between compartments.

Each of these techniques offers advantages in some area while suffering from disadvantages in others. The most common problem is that few models consider myelinated fibers and those that do don't take into account the non-uniformity of myelin to axon diameter ratio, or the different water diffusion profiles between intra-axonal, myelin, and extra-axonal compartments. Computer models can either represent fibers in a honeycomb arrangement with potentially crossing geometries, or represent randomly distributed parallel fibers but not both. In addition no work published so far has modeled glial cells, with the sole exception of DMS, but it does not

clarify how they are included in the geometry, i.e. spatial distribution and axon-to-glia ratio, and how they affect DTI acquisition. Finally, while some software phantoms and computer methods offer high flexibility in tuning the geometry, no studies made use of this feature to simulate demyelination, gliosis and axon compaction. The FiberBlender system presented in the next chapter will address all of these challenges.

III. FIBERBLENDER SIMULATION SYSTEM

Recreating an anatomically accurate computer representation of a nerve bundle with all its intricate details is a daunting task that requires making several assumptions about the microstructure. Nevertheless, for the purpose of simulating particle diffusion, the problem can be reduced to only modeling the different components affecting the diffusion i.e., axons, myelin, and glial cells. FiberBlender takes a similar approach to the Fiberfox phantom with user drawn fibers and glia. However this manual operation is limited to only producing small base models that are in turn used as building blocks to programmatically generate the complete structure, and it does not require extensive neuroanatomical knowledge as long as the base models meet a set of baseline criteria in terms of cell shape, distribution, density, and geometry. For this reason, the chapter begins with a description of the anatomy of axons, myelin, and glial cells as design goals for modeling strategies. This is followed by an overview of the complete FiberBlender framework from modeling, to diffusion simulation, and NMR signal acquisition. The final sections describe some baseline simulation experiments to assess the validity of the system.

3.1 Properties of Basic Elements

3.1.1 Axons

From Fig. 3.1-b, the primary observations to make about a fiber bundle are the compactness of the geometry and the random spatial location of axons. While some existing models were capable of reproducing some of those aspects, they generally rely on a single axon distribution profile and do not account for either the variation in axon diameter, or the presence of a myelin sheath and glial cells. Axon density and size distributions not only depend on the region of the brain but can also vary between subjects further increasing the complexity of the system [99].

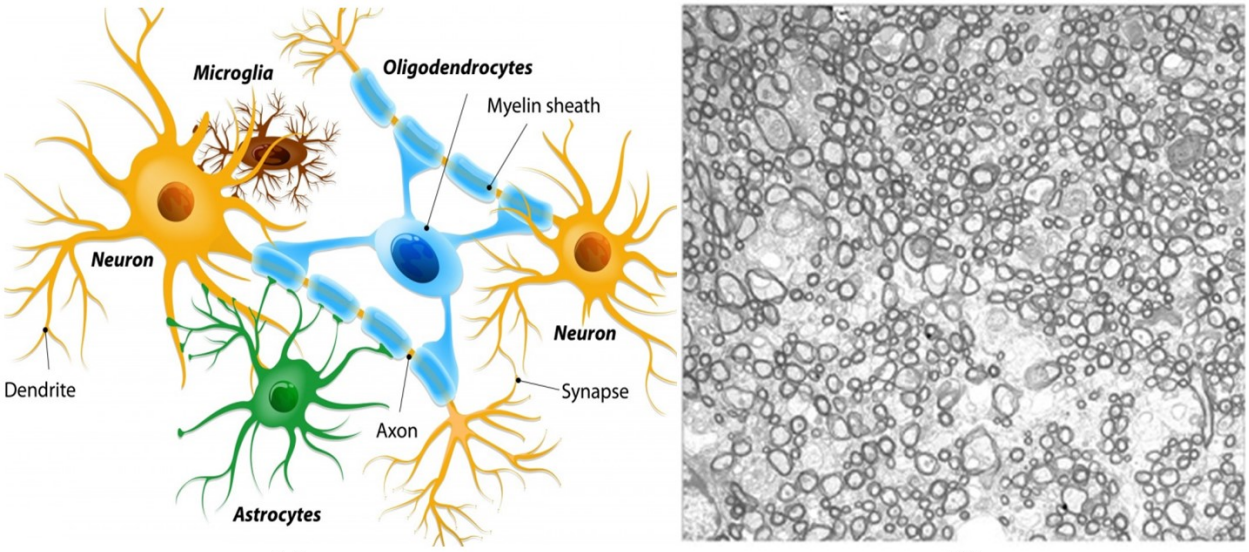

Fig. 3.1: (a) Basic elements of a fiber bundle with neurons (orange), myelin (blue), and glial cells (green and blue) [104]. (b) Example of an electron microscopy image of the mouse corpus callosum [101].

Once again the most reliable data is collected from microscopy images on humans, primates and rats [100 - 103]. Studies have shown that axon diameters tend to follow a gamma or Gaussian distribution, although measurements reported by Sepehrband [101] show that in certain regions of the brain diameters follow a generalized extreme value distribution. The largest axons are located in the center of the corpus callosum (CC) with mean diameters above 6μm whereas in other regions mean diameters may be as small as 0.5μm. Axon density also varies with typical axon volume fractions comprising between 50% and 60% for combined axon and myelin. The intra-axonal space, or axoplasm, is not entirely hollow and contains neurofilaments, microtubules, and mitochondrion but these elements can be ignored as they do not have a significant role in the intra-axonal diffusion [63]. Therefore in the context of diffusion, axons are represented as hollow oblong shaped cylinders.

3.1.2 Myelin

The myelin sheath is a vital component in many mature neurons and is fundamental to the efficiency of neural transmissions by acting as an electrical insulator to speed up action potential conduction [105]. Its degeneration (demyelination) or abnormal formation (dysmyelination) afflicts the conductivity of neural transmissions and leads to poorer cognitive performance generally seen with MS patients and in post-chemotherapy. Myelin is formed by different types of glial cells, in the CNS their growth is supplied by oligodendrocytes (Fig. 3.1-a), whereas in the peripheral nervous system this role is assumed by Schwann cells. However, not all axons in the brain are myelinated, and similarly to axon diameters, the degree of myelination and the relationship between myelin thickness and axon size varies between different brain regions as well as among subjects. Studies even suggest that neural tracts experience rapid myelin changes as the brain reinforces certain connections due to learning and memory formation as evidence of the plasticity of neurons [107]. The g-ratio (Fig. 3.2-a) defined as the ratio between the inner and outer diameter of an axon is typically used to measure the degree of myelination in an ROI [106, 108]. For normal neurons in the CNS, mean g-ratio ranges from 0.6 to 0.68 but the correlation between axon diameter and myelin thickness is non-linear [109]. This relationship is shown in Fig 3.2-b with data sampled from several macaque brains [106]. For the smallest axons ($< 1\mu m$) the g-ratio is around 0.5 or 50% of the total axon diameter, then from 0.6 to 0.8 in the mid-range (1-4μm), and is around 0.8 for the largest axons ($> 4\mu m$) or 20% of the total axon diameter. The myelin sheath is not a single layer but is made up of a spiraling arranged lamellae wrapping around the axon. However in FiberBlender as with other models, their representation is simplified as a single layer since the nature of radial water diffusion between myelin layers is not

well understood. The myelin sheath can be modeled as a second concentric cylinder around the main axon.

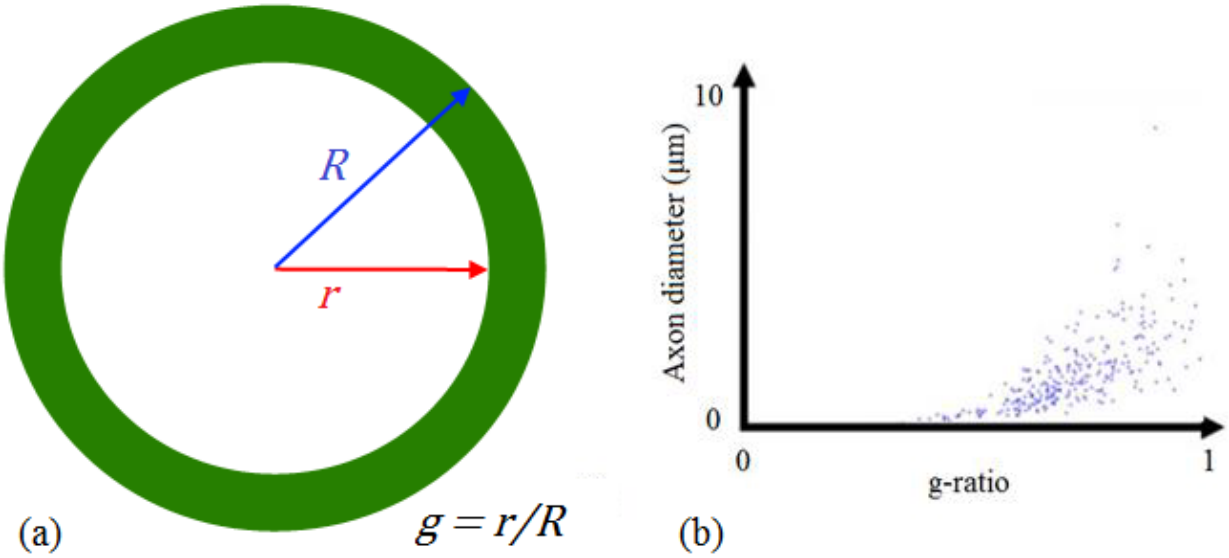

Fig. 3.2: (a) Representation of a myelin sheath wrapping around an axon. (b) Correlation between axon diameter and myelin g-ratio [109].

3.1.3 Glials

There are two types of glial cell in the CNS, microglia and macroglia of which oligodendrocytes (Fig. 3.1-a) and astrocytes are the largest and most abundant [110], therefore only these two will be modeled in FiberBlender. These cells are star shaped because of their numerous processes radiating in all directions that extend up to 50µm. Oligodendrocytes spread their processes around axons and are responsible for the development of the myelin sheath as shown in Fig. 3.1-a. Astrocytes have numerous functions including axon repair. Consequently they serve a key role in the brain despite being often overlooked or misunderstood. For the purpose of diffusion, only the soma (cell bodies) need to be modeled and can be represented as oblong ellipsoids. The size of glial cells and their ratio with respect to axons varies between different regions of the brain and has long been misunderstood by researchers. The soma of

oligodendrocytes in cerebellar white matter is generally accepted to be around 10μm whereas astrocytes are slightly smaller (~5μm) [111]. However the number of glial cells in the brain is still the subject of debate with older experiments showing a 10:1 glia to neuron ratio (GNR) whereas more modern estimates put this much lower to a 1:1 relationship with statistics heavily dependent on the region of the brain under investigation [110].

3.2 Building Fiber Bundles

The problem of generating an axon bundle inside a cubic voxel can be likened to filling a square with a maximum number of circles without overlaps. In algorithms this is known as the two-dimensional circle packing problem and is easily solvable, one optimal solution is a hexagonal array of circles which is used in other modeling strategies. However this becomes much more complex when considering circles with arbitrary diameters. This is known as the Arbitrary Sized Circle Packing Problem (ACP) and is a classic example of non-deterministic polynomial-time or NP hard optimization problem. While some solutions have been proposed for ACP using heuristic approaches, none have been defined with the following additional constraints:

- Oblong-shaped circles.
- Random spatial locations.
- Circle diameters must following a specific distribution.

The exact mathematical definition for each of these constraints is difficult to determine and indeed a computational solution may not even exist. Yet in order to overcome the shortcomings of previous modeling strategies and create more realistic axon bundles, FiberBlender models of axon and glial cells must meet these criteria. For this reason the system relies on custom drawn

base models that can represent the above restrictions and are used as the primary building blocks to generate larger axon configurations.

3.2.1 Base Models

Base models consist of small bundles of axons and glia created manually with Blender. These models are comprised of hollow oblong-shaped cylinders and ellipsoids to represent myelinated axons and glial cells respectively (Fig 3.3). They can be combined and reshaped to form voxels with larger structures in any desired configuration. An initial set of 20 base models is created with axon sizes in ascending order such that each model forms a bin of a certain diameter. For example the first two models contain axons with diameters between 0 and 1μm, the next two contain axons with diameters between 1μm and 2μm and so on. In practice a diameter of 0 is not possible so the smallest axons are 0.2μm in diameter with dimensions given in terms of total diameter (combined axon and myelin). All base models are 10x10x10μm, two examples are shown in Fig. 3.3 for two base models with differently sized axons. The originality of this approach is that no two base models and in fact no two axons in the set are alike. The base models are also designed in this fashion to exemplify both the compactness and random spatial location of axons and glia. This randomness is extrapolated when generating larger structures to account for the tortuosity of the fibers, and to generate diverse models representing the variability among subjects. On average the combined axon, myelin, and glia volume fraction is around 68% while the extra-axonal volume fraction is 32% for all models. Myelin volume fraction controlled by the g-ratio is a user defined variable. Other variables are the distribution of axon diameters and the glia to axon ratio initialized as 1:1 in the base models but can be increased as needed. These values are set when forming the larger structure.

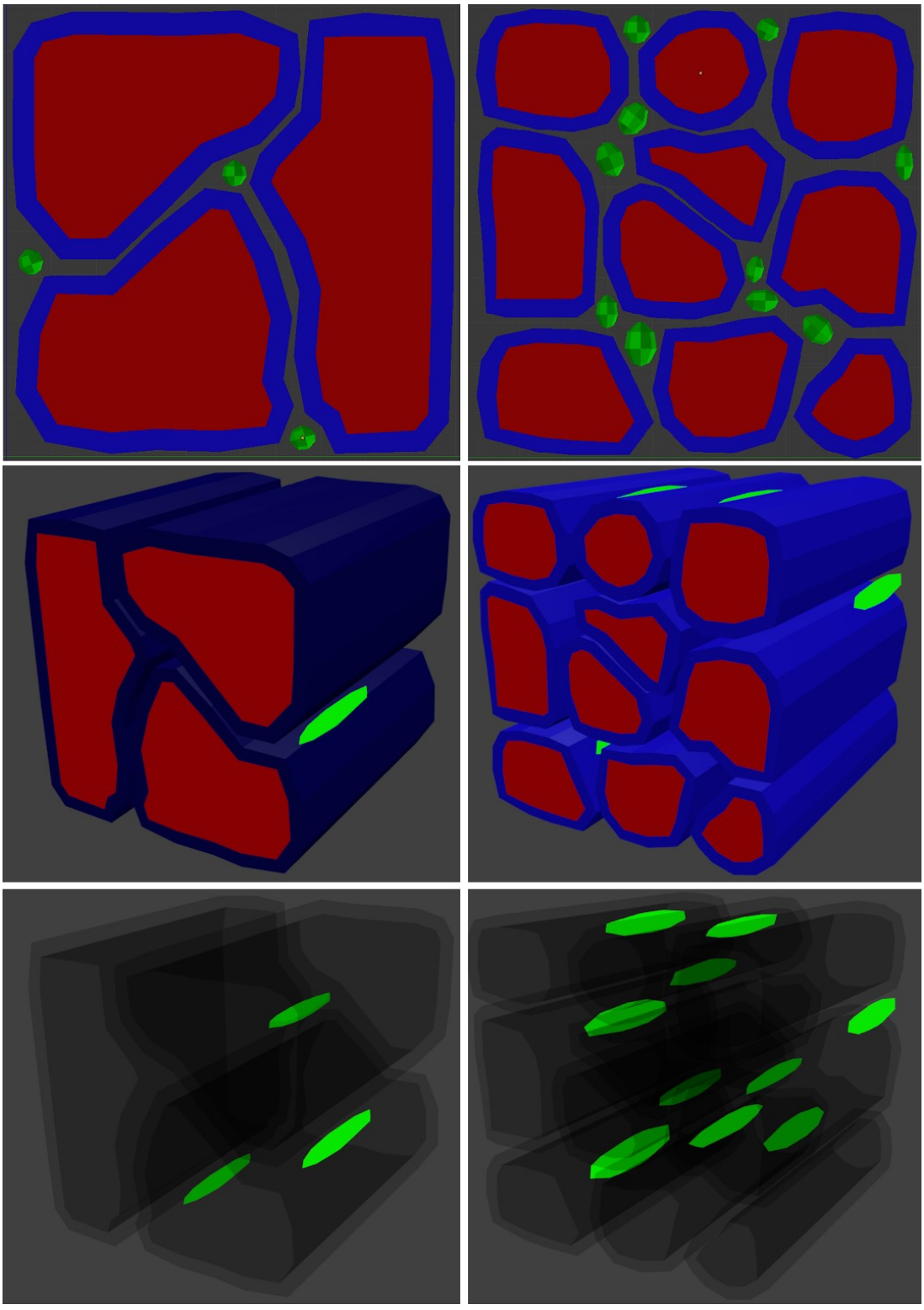

Fig. 3.3: Example of two base models (6μm left column and 3μm right column). Axons, myelin, and glial cells are highlighted in red, blue, and green respectively.

3.2.2 Generating the Structure

Fiber generation is an iterative process where base models are combined to form a voxel. It begins by selecting M samples from the set of 20 base models such that the sample set corresponds to user defined input variables. These are: i) the dimensions of the voxel (d_x, d_y, d_z) that determine the sample size ($\mathrm{M} = \mathrm{d}_y \times \mathrm{d}_x/10$), ii) the distribution type of axon diameters with corresponding parameters as one of Gaussian (mean μ, standard deviation σ), gamma (shape α, scale β), or generalized extreme value (location μ, scale α, and shape β), iii) the myelin g-ratio that determines the myelin volume fraction, iv) the glial to axon ratio (GNR). The models are sampled such that the axon diameters from all M samples correspond to the target distribution. Models are initially placed adjacent to one another in the yz plane, or along the x direction, and can be rotated by a factor of 0°, 90°, 180°, or 270° to further increase the randomness of the structure. This forms a layered axon structure as shown in Fig. 3.4. This example contains ~1400 axons, with the main body and myelin highlighted in red and blue respectively, and ~2800 glial cells uniformly distributed across the space highlighted in green.

In case of crossing fibers each layer is rotated to correspond to a different direction, with additional inputs for the angle of crossing, and a second axon diameter distribution since each direction may have differently sized axons.

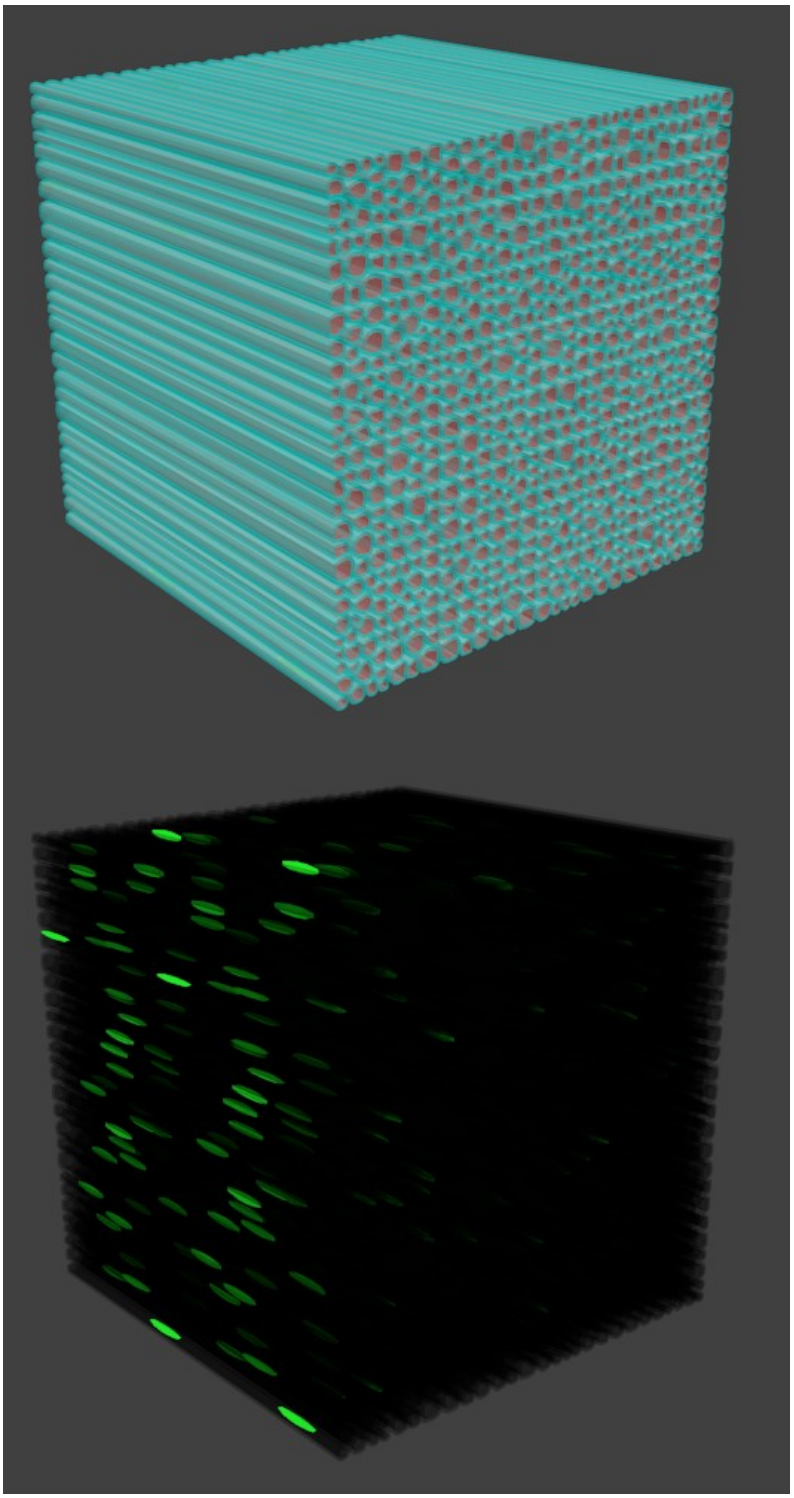

Fig. 3.4: Example of a 100×100×100µm fiber structure with highlighted axon body and myelin (red and blue top figure) and glial cells (green bottom figure).

3.3 Diffusion Simulation

A key feature in Blender is its particle system. Particles are generated across the voxel and are located either in the extra-axonal space (between axons), within the myelin layer, or in the intra-axonal space (inside individual axons). Their spatial distribution however is not uniform with 60%, 30% and 10% of particles present in the extra-axonal, intra-axonal, and myelin respectively. A Brownian force causes them to move and interact with the surrounding axons and glia boundaries creating a hindered and restricted diffusion. The diffusion coefficient D of water molecules ranges from 1 to 3 mm^2/s at body temperature (37ºC). However in Blender there is no single variable to directly regulate the diffusion rate, this is controlled by a set of dimensionless parameters. In addition, the Sequential Impulse Solver algorithm that computes physics in Blender has low predictability and any small changes in the initial conditions of the system, such as a particle's initial position, results in large variations. Therefore before each simulation is performed, the system needs to be properly calibrated in order achieve a desired diffusion rate. For this purpose a free diffusion calibration test is devised where particles move in an isotropic setting with no obstacles or boundaries. In this environment, the theoretical amount of particle displacement can be estimated from (2) $< x^2 >= nD\Delta t$ using Einstein's relation. For the calibration test, N particles are generated over the simulation space and are diffused over a period Δt. Each particle's displacement vector x_i is recorded, representing the total distance traveled by each particle i. The experimental $< x^2 >$, also called the expectation value, can be calculated from

$$< x^2 >= \frac{\sum_{i=1}^{\mathrm{N}} {x_i}^2}{\mathrm{N}}. \tag{16}$$

Using these definitions, Blender's diffusion parameter can be calibrated such that the experimental expectation value closely approximates the theoretical value from (2) for a desired diffusion coefficient D. For example, to obtain a diffusion rate of D = 2.6μm^2/ms over 100ms with n = 6, the square root expectation value from (2) yields $< x^2 >$ = 39.496, and Blender's parameters are calibrated to approach the same value from (16). This is illustrated in Fig. 3.5 where the system is calibrated to closely approximate a diffusion rate of 2.6mm^2/s.

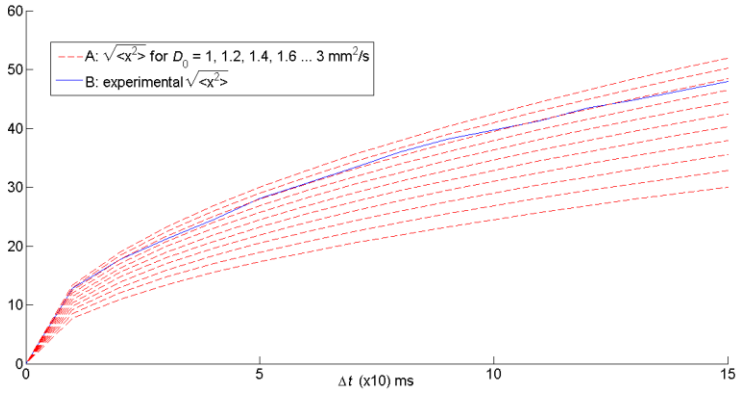

Fig 3.5: Calibration of the experimental expectation value (blue curve) calculated from (16), to the theoretical value (red curves) obtained from (2).

3.4 Extracting DTI Measurements

With the working model and diffusion simulation in place, the next stage is to extract NMR signals to compute the ADC, the diffusion tensor, and other measurements. Within Blender's framework, the system does not emit RF pulses to magnetize the particles, and the particles in turn do not possess a spin to get magnetized and emit NMR signals, they simply act as inert objects with infinitesimal size diffusing inside the simulation space. Therefore signals cannot be simulated or measured by the conventional approach. Stejskal and Tanner's method showed that the attenuation in NMR signal, calculated in (12), is due to a phase shift proportional to a

particle's diffusion. Therefore, signals can be obtained by calculating each particle's accumulated phase from the displacement vectors obtained during the simulation.

3.4.1 Measuring the ADC

Recalling the previous chapter's discussion (Fig. 2.8), in the absence of gradients the magnetic field is uniform such that all the particles precess at the same rate and a particle's phase is relative to the static field $\boldsymbol{B}_0$ such that $\varphi(t) = \gamma \boldsymbol{B}_0 t$ [112]. When a gradient of strength g and duration δ is applied, the distance r_i traveled by each particle i induces a phase shift given by

$$\varphi_i(t) = \gamma \boldsymbol{B}_0 t + \gamma g \int_{t_1}^{t_1+\delta} r_i(t)dt. \tag{17}$$

With a PGSE sequence, two gradients are used producing a phase shift relative to each period. Therefore at the end of the sequence (t = TE) the total shift for each particle is given by

$$\begin{aligned} \varphi_i(\mathrm{TE}) &= \left\{\gamma \boldsymbol{B}_0 t + \gamma g \int_{t_1}^{t_1+\delta} r_i(t)dt\right\} - \left\{\gamma \boldsymbol{B}_0 t + \gamma g \int_{t_1+\Delta}^{t_1+\Delta+\delta} r_i(t)dt\right\} \\ &= \gamma g \left\{\int_{t_1}^{t_1+\delta} r_i(t)dt - \int_{t_1+\Delta}^{t_1+\Delta+\delta} r_i(t)dt\right\}. \end{aligned} \tag{18}$$

Here r refers to the longitudinal displacement measured along the direction of the gradient only, since a transverse translation does not result in any change in magnetization. Looking back at the PGSE sequence in Fig. 2.7, (18) shows how the first integral relates to the phase accumulated during the first gradient pulse, while the second integral relates to the phase accumulated during the second gradient pulse. For an ensemble of particles, the diffusion profile is generally approximated as Gaussian producing a Gaussian distribution of phases [112]. With these considerations, the normalized attenuation of the echo signal is calculated by

$$S = S_0 \int_{-\infty}^{\infty} \mathrm{P}(\varphi, \mathrm{TE}) \cos\varphi \, dt, \tag{19}$$

where $\mathrm{P}(\varphi, \mathrm{TE})$ is the phase distribution function. By definition it must be a normalized function such that $\int_{-\infty}^{\infty} \mathrm{P}(\varphi, \mathrm{TE}) dt = 1$. Therefore the integral in (19) is the expected value of the cosine of the phases, and assuming the distribution to be Gaussian, it is rewritten as

$$S = S_0 \frac{\sum_{i=1}^{\mathrm{N}} \cos\varphi_i}{\mathrm{N}}, \tag{20}$$

for a discrete number of particles N. The attenuation signal was defined as $S = S_0 e^{-bD}$ in (12), hence the ADC is found by combining the right hand sides of (12) and (19), and performing the natural logarithm to solve for D_{app}

$$S_0 e^{-bD_{app}} = S_0 \frac{\sum_{i=1}^{\mathrm{N}} \cos\varphi_i}{\mathrm{N}},$$

$$D_{app} = -\ln\left\{\frac{\sum_{i=1}^{\mathrm{N}} \cos\varphi_i}{\mathrm{N}}\right\} / \, b, \tag{21}$$

3.4.2 Calculating the Tensor and DTI Metrics

To obtain a diffusion tensor, this process is repeated for at least six gradient directions by acquiring the ADC for each one. [113] introduces the vectors

$$\bar{\mathrm{D}} = \left[D_{xx} \;\; D_{yy} \;\; D_{zz} \;\; D_{xy} \;\; D_{xz} \;\; D_{yz}\right]^{\mathrm{T}}, \tag{22}$$

as a reformulation of the tensor in (16) and

$$\bar{\mathrm{g}}_k = \left[g_x^2 \;\; g_y^2 \;\; g_z^2 \;\; 2g_x g_y \;\; 2g_x g_z \;\; 2g_y g_z\right]^{\mathrm{T}}, \tag{23}$$

corresponding to each gradient direction k. The tensor equation is now expressed as

$$\bar{\mathrm{g}}_k^{\mathrm{T}} \cdot \bar{\mathrm{D}} = D_{app_k} \;\; (k = 1, \ldots, K; K \geq 6). \tag{24}$$

This system can be rewritten in matrix form:

$$\mathbf{A}\bar{\mathrm{D}} = \mathbf{B}, \tag{25}$$

where $\mathbf{A}$ is the k x 6 matrix

$$\mathbf{A} = \begin{bmatrix} \bar{\mathrm{g}}_1^{\mathrm{T}} \\ \vdots \\ \bar{\mathrm{g}}_k^{\mathrm{T}} \end{bmatrix} = \begin{bmatrix} g_{1_x}^2 & g_{1_y}^2 & g_{1_z}^2 & 2g_{1_x}g_{1_y} & 2g_{1_x}g_{1_z} & 2g_{1_y}g_{1_z} \\ \vdots & \vdots & \vdots & \vdots & \vdots & \vdots \\ g_{k_x}^2 & g_{k_y}^2 & g_{k_z}^2 & 2g_{k_x}g_{k_y} & 2g_{k_x}g_{k_y} & 2g_{k_y}g_{k_z} \end{bmatrix}, \tag{26}$$

and $\mathbf{B}$ is a k-dimensional vector of ADC values,

$$\mathbf{B} = \begin{bmatrix} D_{app_1} & \cdots & D_{app_k} \end{bmatrix}^{\mathrm{T}}. \tag{27}$$

It is worth noting that matrix $\mathbf{A}$ is solely dependent on the choice of gradient directions, while $\mathbf{B}$ is a vector of ADC maps. The solution to (25) is given by the pseudo-inverse of matrix $\mathbf{A}$

$$\bar{\mathrm{D}} = \mathbf{A}^{+}\mathbf{B} = (\mathbf{A}^{\mathrm{T}}\mathbf{A})^{-1}\mathbf{A}^{\mathrm{T}}\mathbf{B} \tag{28}$$

The diagonalization of the diffusion tensor yields three eigenvectors and three eigenvalues (λ_1, λ_2, and λ_3) representing the magnitude of diffusivity in the axial direction (AD = λ_1) and radial direction (RD = $(\lambda_2 + \lambda_3)/2$), with the mean diffusivity given as the average of all three (MD = $(\lambda_1 + \lambda_2 + \lambda_3)/3$). The fractional anisotropy (FA) is calculated as

$$\mathrm{FA} = \sqrt{\frac{2}{3}} \cdot \frac{\sqrt{(\lambda_1 - \mathrm{MD})^2 + (\lambda_2 - \mathrm{MD})^2 + (\lambda_3 - \mathrm{MD})^2}}{\sqrt{\lambda_1^2 + \lambda_2^2 + \lambda_3^2}} \tag{29}$$

3.5 Noise Propagation in MRI

MRI scanners are susceptible to noise that propagates through the system starting from the patient's body to the image formation. The origin of noise can be related to two components: noise from the scanner apparatus and noise from the patient's body inside the scanner [114]. Any electrical resistance generates a thermal noise called Johnson–Nyquist noise, which is also generated by the human body as a consequence of the ionic nature of body tissue and fluids. To

be more specific about the sources of circuit resistance consider the equivalent circuit of an RF receiver coil in Fig. 3.6. The coil typically made of copper has resistive losses, represented by R_c, that produce electrical noise. In addition when a human subject is placed inside the scanner, the coil acquires additional resistance R_s. The magnetic flux from the particles induces the NMR signal represented as a sinusoidal voltage source V_{sig}. This signal must compete with the noise voltage from the equivalent resistances V_n.

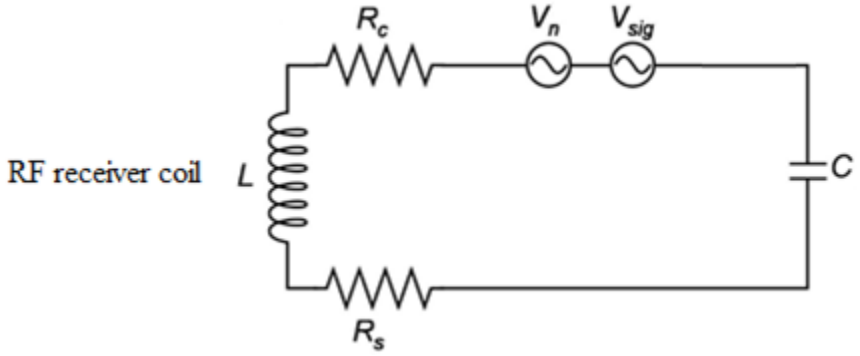

Fig. 3.6: Circuit equivalent of a RF receiver coil L with noise producing resistances R_c and R_s inducing a noise signal V_n.

This essentially produces white noise with zero mean and Gaussian amplitude distribution. Consequently when mapped to the k-space frequency domain the noise signal follows the family of Rician distribution as many studies have shown [114]. In the FiberBlender noise can be added to the signal in (20) by a complex Gaussian term η with mean zero, constant standard deviation and independent real and imaginary parts such that

$$S = S_0 \frac{\sum_{i=1}^{\mathrm{N}} \cos \varphi_i}{\mathrm{N}} + \eta. \tag{30}$$

With this formulation, η can be controlled to generate data for different levels of SNR which is defined as the ratio of mean μ to standard deviation σ of a signal acquisition,

$$\text{SNR} = \frac{\mu}{\sigma}. \tag{31}$$

3.6 Baseline Experiment

A baseline experiment is performed on the model produced in Fig. 3.4 to demonstrate the capacities of FiberBlender in reproducing true DTI data. The model represents a 100×100×100μm cubic voxel with parallel axons following a gamma distribution with mean diameter of 3μm (shape parameter α = 3 and a scale parameter β = 1). The generated output volume contains ~1400 axons with diameter statistics in Fig. 3.7 and ~2800 glial cells. The simulation is run for 50,000 particles scattered across the volume such that particles in the extra-axonal and intra-axonal space diffuse at a rate of D = 2.5mm^2/s, and myelin particles diffuse at a rate of D = 1.2mm^2/s. Data is acquired using a Stejskal-Tanner or PGSE sequence with the following parameters: TE = 120ms, δ = 19ms, Δ = 56ms, and b = 1000s/mm^2 (from (13) this is the equivalent of applying a gradient strength of g = 29.77T/mm).

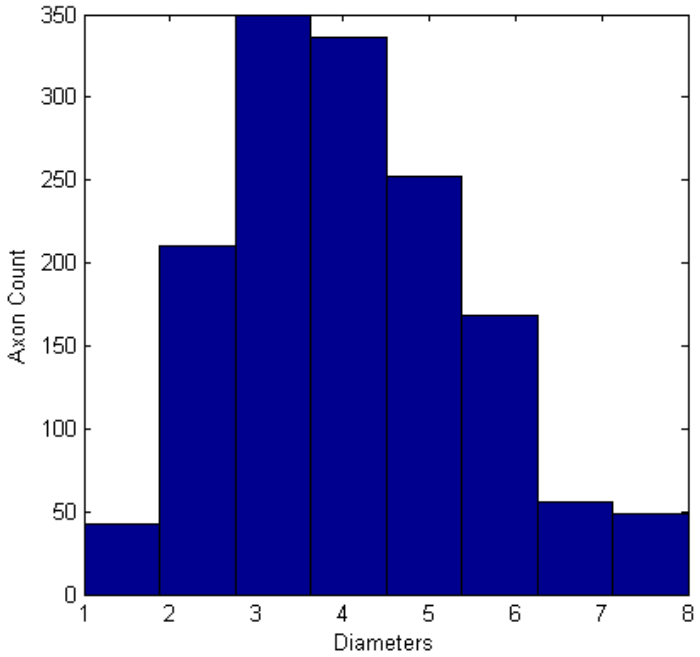

Fig 3.7: Histogram of axon diameter distribution in the generated output volume.

When the simulation ends, the coordinates of each particle are recorded to calculate the displacement vectors r_i and compute the ADC following the steps detailed in section 3.5. The simulation is then repeated for a total of 20 gradient directions with each direction using a new sample of particles starting at different initial locations. The data from 20 directions is used to calculate the diffusion tensor and DTI metrics with results displayed in Table 2 for different SNR levels. Since FiberBlender is able to isolate the particles from each water compartment, the noiseless tensor from each one is represented in Fig. 3.8.

Table 2. DTI metrics for the baseline experiment.

	Noise Free	SNR = 30	SNR = 10
MD ($\times 10^{-3}$) mm^2/s	0.823	0.842	0.832
AD ($\times 10^{-3}$) mm^2/s	1.861	1.911	1.945
RD ($\times 10^{-3}$) mm^2/s	0.327	0.323	0.293
FA	0.791	0.805	0.832

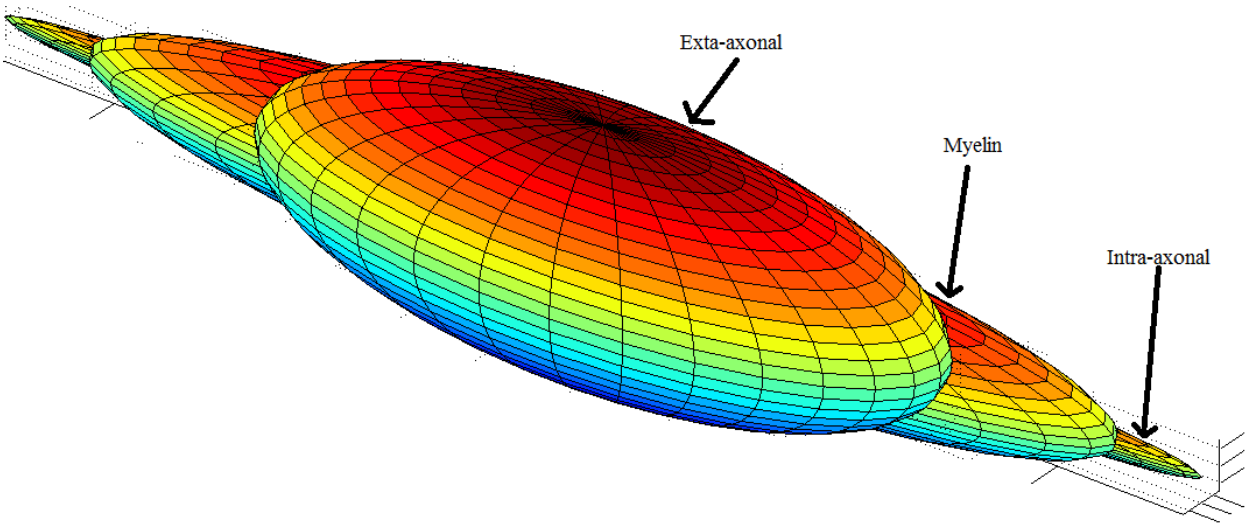

Fig. 3.8: Diffusion tensors for each water compartment measured in the baseline experiment.

A visual interpretation of the tensor demonstrates how the extra-axonal diffusion is hindered, and is therefore more isotropic than other compartments since particles can travel throughout the simulation space. In the case of myelin and intra-axonal water the diffusion is restricted, as outlined by the heavily directional tensors. One noticeable difference is that myelin water is less directional than intra-axonal since it can travel in more radial directions. This signifies that orientation information is mostly obtained from intra-cellular particles. Table 2 also demonstrates how low SNR biases diffusion measurements, especially the FA.

IV. OPTIMIZING DTI ACQUISITION TO CAPTURE DEMYELINATION

Chapter 3 laid the groundwork for the FiberBlender system, and this chapter takes a closer look at the case of demyelination, a common symptom for many neurodegenerative disorders. The chapter begins with a short physiological description of demyelination and how it affects the corpus callosum (CC) region of the brain. An acquisition sequence optimization is then introduced to better capture the effects of demyelination on DTI metrics with results shown for several non-identical models. Finally the chapter looks at gliosis and axon compaction which are often related to demyelination, and how to properly differentiate them.

4.1 Demyelinating Diseases

Myelin insulation around the axons plays an important role in cognitive performance as it maintains the conductivity and reliability of neural transmission. MS, an autoimmune disease damaging the CNS, is understood to be the most common cause of demyelination affecting millions worldwide. More recently attention turned to long term effects of chemotherapy as another source of delayed demyelination. Yet many more disorders are also known to result in demyelination (e.g. disturbances of blood flow, edema, brain injury), each having different underlying mechanisms [116]. For example MS is diagnosed as one of four types, the relapsing-remitting (RR) case is the most common form found in approximately 85% of patients [117]. This is characterized by temporary episodes called relapses or flare-ups when symptoms appear for periods of at least 24 hours, followed by remissions when patients recover. Physiologically, these relapses are caused by attacks from the body's immune system on oligodendrocytes that result in demyelination, while during remissions new oligodendrocytes and astrocytes are created to repair the damaged myelin and axons resulting in temporary gliosis and remyelination. On the

other hand, other types of MS are more chronic and exhibit steadily worsening symptoms and disease state without remission, with the implication that the demyelination is constant with no apparent gliosis or remyelination. This is similar to chemotherapy where toxins prevent the formation of new glial cells. Therefore many neurodegenerative disorders may cause demyelination in different manners and while conventional MRI imaging can reliably capture in vivo brain lesions from MS, the origin of symptoms can be often difficult to confirm since these signs may be similar to those of other medical conditions [118].

With DTI's inception, research began on employing the new technology to observe demyelination with quantitative parameters such as FA and MD for a better assessment of the extent of tissue damage outside of plaques detected by conventional MRI. Multiple studies proved a significant association between increasing RD and decreasing FA on one side, and the amount of detectable lesions on the other, suggesting that the diffusion becomes more isotropic after myelin loss. Diffusivity measurements are usually accompanied by cognitive performance tests such as verbal fluency, math, reading, and memory, to establish a correlation between decreasing FA and overall lower cognitive functions as evidence of demyelination.

The common interpretation is that higher FA is indicative of better myelin integrity and neurocognitive functions, while lower FA signifies the opposite. Yet comprehensive findings are hard to obtain as they require longitudinal studies spanning several years with multiple subjects and control groups. Some research even contradict the established consensus where higher FA did not correspond to better cognition, hypothesizing that FA changes might be resulting from gliosis or axon compaction but this is yet to be proven [119 - 120]. The goal of the experiments in this chapter is to simulate different demyelination, gliosis and axon compaction to differentiate these conditions to understand how each one affects DTI.

4.2 Demyelination Gliosis and Compaction in the Corpus Callosum

Studies of demyelination are most common in the CC, a flat bundle of fibers connecting the two hemispheres of the brain (Fig. 4.1), since this indicates that the pathological mechanisms of demyelination are widespread and interrelated throughout the brain. The CC is generally divided into 3 sections shown in Fig. 4.2, the genu is closest to the front of the brain, the mid-section called isthmus or body which has the largest axons in the brain, and the splenium at the back.

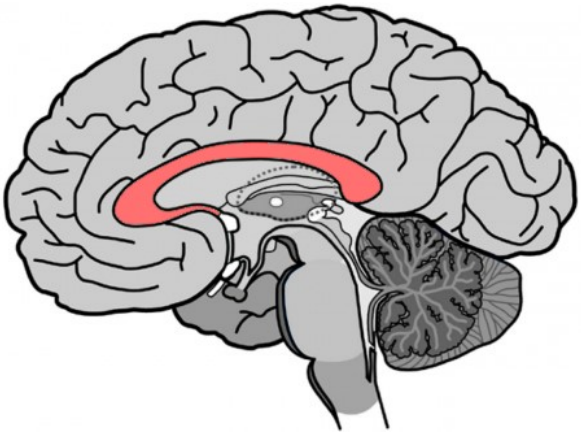

Fig. 4.1: Midsagittal view of the brain with the location of the CC highlighted in red.

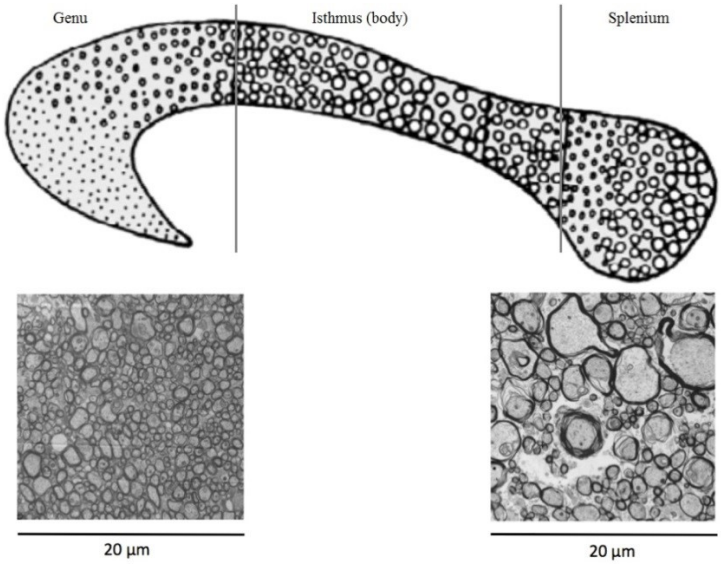

Fig. 4.2: Visual representation of axon diameter distribution in each section of the CC [102].

Each section contains axons with a different size distribution; in the body axons are generally considered Gaussian distributed, while the genu and the splenium may have a gamma or generalized extreme value distribution. Therefore modeling the CC consists of generating parallel axons with the appropriate size distribution. Studies have also shown regional differences of glial cell numbers [121]. Glial cell density decreased for the genu and the body, while a minor increase is observed for the splenium. However the exact glia to axon numbers ratio could not be determined accurately with estimates around 2.5:1 and 4:1. Similarly, the myelin g-ratio is not constant across the CC with the most recent studies finding higher values in the splenium and lower values in the body and genu [122]. Thus in the forthcoming simulations, glia to axon ratios are maintained at 4:1 for the splenium and 3:1 for the body and genu, while the g-ratio is set at 0.72 for the splenium and 0.66 for the body and genu. Since these values are functions of human age and sex, they are in no way representative of every subject, but form an acceptable average. Furthermore, the goal of the simulations is to capture the relative change in myelin thickness and glia density not necessarily the exact figures.

The rate of demyelination is the same for all axons regardless of size and location. A demyelination function in FiberBlender performs a stepwise percentage reduction of the original myelin width. Fig. 4.3 demonstrates a demyelination effect in a cross section of parallel axons where the thickness is reduced to 50% its original width. A noticeable consequence of this is the expansion of the extra-axonal space which will inadvertently alter the diffusion process and DTI measurements. Similarly, axon compaction is also stepwise function accomplished by moving the axons and glial cells progressively closer toward the voxel center until an overlap is detected. Gliosis is performed by duplicating each glial cell in the volume, and redistributing them in the longitudinal direction.

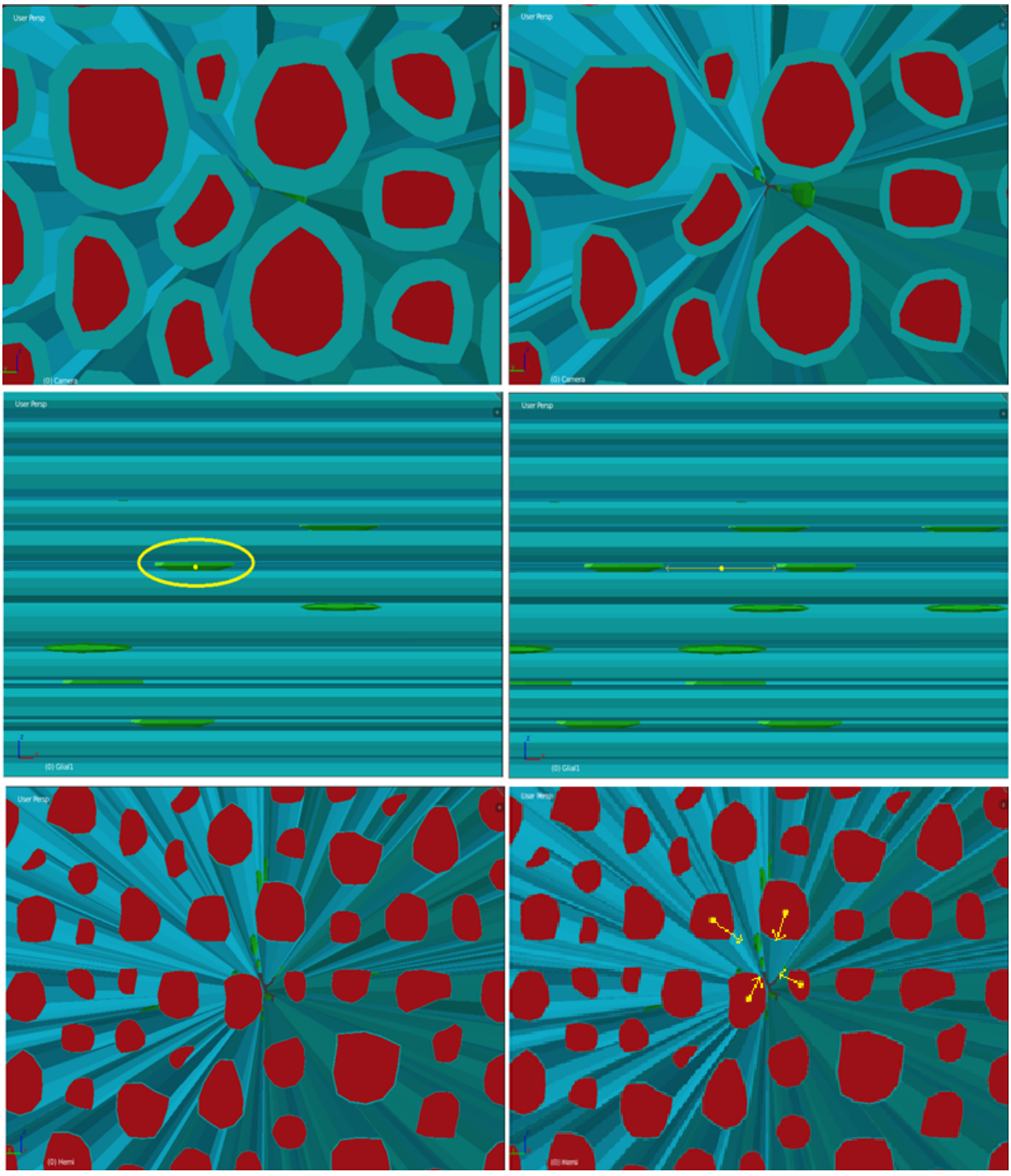

Fig. 4.3: (Top) Cross sectional view of axons demonstrating a demyelination from full myelin to 50% original thickness. (Middle) Transverse view of gliosis where each glial cell duplicates. (Bottom) Cross sectional view of axon compaction.

4.3 Strategies for Optimization

DTI optimization efforts have focused on improving image quality and SNR [123 - 125], enhancing the tensor and fiber orientation estimation [126 - 130], or refining the measurement of diffusion metrics (FA, MD, AD, and RD) [131, 132]. These can be made either with hardware by improving the sensitivity and design of coils, or with software by fine tuning sequence parameters. Yet most of the existing methods have considered these different aspects separately, only Gao et. al. [130] has taken a unified optimization approach to simultaneously consider all imaging parameters involved (i.e. SNR, b-value, timing parameters, gradient directions). In addition many methods simply rely on selecting different imaging parameters and comparing the results without defining a cost function with robust algorithms to describe the optimization procedure. This may be due to the difficulty in clearly defining which parameters need to be optimized as they can be specific to a certain scanner or certain model and may not be ideal in different conditions. For this reason optimization strategies must use a variable that is independent of imaging parameters that can quantify the quality of measurements.

4.3.1 The Case for Entropy

While maximizing SNR can be a straightforward goal, choosing imaging parameters that best describe the diffusivity in tissue is highly dependent on the subject and the scanner and in fact an optimal result does not exist under this definition. The question should not be “which parameters are best”, rather “which parameters reveal the most information”. Shannon [133] introduced the concept of information entropy as a way to quantify redundant information in communication operations. The entropy $\mathrm{H}(X)$ of a stochastic information source described by a random variable X is the measure of uncertainty associated with X, and is a property of X’s probability distribution function. Mutual information (MI) quantifies the dependence between two random

variables (X, Y) in terms of information communicated by one variable giving knowledge of the other, and is related to the marginal $\mathrm{H}(X)$, $\mathrm{H}(Y)$ and joint entropies $\mathrm{H}(X, Y)$ of both variables. MI has been used in many applications ranging from communication systems to data mining, as well as biological studies such as measuring redundancy in gene sequences, or resolving image registration in MRI and other medical imaging.

In the context of demyelination, MI can be used to quantify the information between signals received from DTI scans at different levels of myelination. To understand this process, consider a voxel comprising an axon bundle generated with FiberBlender. As the system undergoes demyelination the distribution of phases accumulated by each particle changes. Letting $\{X, Y\}$ be two discrete random variables representing the distribution of phases at two different states of myelination, X and Y are independent and their MI, $\mathrm{I}(X, Y)$ represents the complementary information between each simulation. This is calculated by

$$\mathrm{I}(X, Y) = \sum_{y \in Y} \sum_{x \in X} p(x, y) \log \left(\frac{p(x, y)}{p(x) p(y)} \right), \tag{32}$$

where $p(x)$, $p(y)$, and $p(x,y)$ and the marginal and joint probability density functions of X and Y. Given a large sample of phases $X = \{x_1, x_2, \ldots, x_n\}$ and $Y = \{y_1, y_2, \ldots, y_n\}$ obtained from a diffusion simulation, the densities can be estimated using kernel density estimators. Alternatively MI can be expressed in term of entropy such that

$$\mathrm{I}(X, Y) = \mathrm{H}(X) + \mathrm{H}(Y) - \mathrm{H}(X, Y). \tag{33}$$

Intuitively the change in myelin should result in a change in phase distribution. Therefore the goal of the optimization problem is to find an acquisition sequence that minimizes the amount of redundant information between simulations,

$$\begin{aligned} &\text{minimize} \quad : \quad \mathrm{I}(X,Y) \\ &\text{subject to} \quad : \quad \delta < \Delta,\ \delta + \Delta < \mathrm{TE}, \text{ and } 60 < \mathrm{TE} < 120 \end{aligned} \tag{34}$$

Clearly *I(X,Y)* is not directly a function of sequence parameters δ, Δ, and TE, but these values determine the resultant phase distributions *p(x)* and *p(y)*. The constraints for TE are not theoretically necessary but are forced on the system since some acquisition parameters are physically unrealizable with some scanners. In addition δ and Δ are dependent on the type of scanners and cannot be initialized to any arbitrary real value. Therefore these parameters are quantized into a finite set of industry standard values. In turn the solution search space is finite and solved heuristically rather than with an exhaustive minimization algorithm. Hence instead of a global solution for (34), a performance evaluation of different acquisition schemes is provided.

4.4 Simulation Results

Experiments are performed on several structures representing the different regions of the CC. Nine models are generated in total, using three for each region (genu, body, and splenium), with random axon locations as previously described such that no two models are identical. The structural input parameters used to generate each structure are chosen to represent a realistic brain-like environment with the largest axons found in the body and the smallest in the genu. Table 3 summarizes these parameters.

Table 3. Structural parameters for the each region of the CC.

Region	Axon Distribution	g-ratio	GNR
Genu	Gamma (α = 1.5, β = 1)	0.66	3:1
Isthmus (Body)	Gaussian (μ = 7, σ = 1.5)	0.66	3:1
Splenium	Generalized extreme value (μ = 3.5, α = 1, β = 0.5)	0.72	4:1

Simulations are performed using a constant diffusion coefficients of $D = 2.6\text{mm}^2/\text{s}$ for the extra-axonal and intra-axonal particles, and $D = 1.4\text{mm}^2/\text{s}$ for myelin, using a total of 50,000 particles. Simulation duration is determined by the type of acquisition sequence. All simulations use a PGSE sequence with 30 gradient directions. Since timing parameters δ and Δ are dependent on the type of scanners and manufacturer requirements, there is no formally defined method to regulate them and these values are obtained from sources in the literature [71, 86, 87]. In particular, three cases are explored in this study as demonstrated in Fig. 4.4:

- Case A: Short δ short Δ.
- Case B: Short δ long Δ.
- Case C: Long δ short Δ.

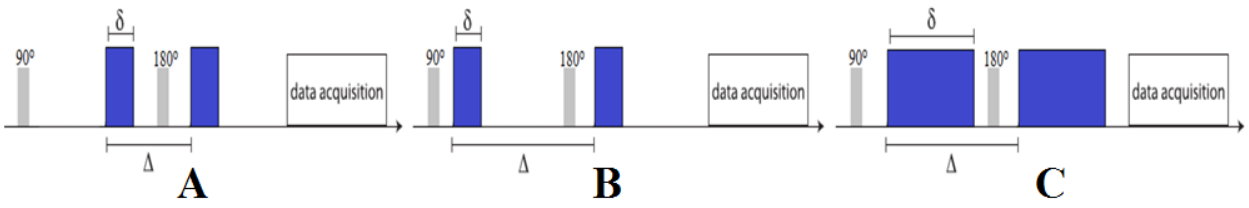

Fig. 4.4: PGSE sequences for cases A, B, and C.

For each case TE values range from 60ms to 120ms with 20ms increments forming the timing input parameters listed in table 4.

Table 4. Timing parameters for cases A, B, and C.

	Case A		Case B		Case C	
TE	$\boldsymbol{\delta}$	$\boldsymbol{\Delta}$	$\boldsymbol{\delta}$	$\boldsymbol{\Delta}$	$\boldsymbol{\delta}$	$\boldsymbol{\Delta}$
120	18.9	50	22	63	37	54
100	19	42	19	56	34.75	53.5
80	17.5	31	18	49	31.75	40.75
60	12.9	21.8	14.2	42	21.5	26.5

Experiments are initially obtained for a fixed b-value of b = 1000s/mm^2 resulting in a gradient amplitude g that depends solely on the choice of timing parameters (δ and Δ) obtained from (13). The effect of modifying the b-value, i.e. changing the amplitude g while keeping δ and Δ fixed, is explored in later sections. Demyelination is performed on each model, starting with a fully developed myelin at 100% total width representing a subject in a healthy state, followed by a progressive demyelination where the width is reduced sequentially by 10% until the myelin is completely destroyed. DTI metrics are calculated at each level of demyelination and a pairwise MI is computed from (32) such that X is the phase distribution obtained from a simulation for a healthy state (100% myelin) and Y is the distribution at each subsequent myelin level (90% - 0%), average MI can then be found to represent the amount of information delivered throughout the demyelination process. Optimization is performed by selecting the sequence in table 4 that results in the lowest average MI.

4.4.1 Regional Analysis

Tables 4, 5, and 6 summarize the calculated average MI of the different models of the splenium, genu and body respectively. Experimental results show that sequences for case B which uses shorter pulses δ and longer diffusion times Δ, perform generally better with a slight edge over case A. The difference is much more notable with case C.

Table 4. Average Mutual Information for selected sequences in the CC splenium.

TE	Case A			Case B			Case C		
	Spl. 1	Spl. 2	Spl. 3	Spl.1	Spl. 2	Spl. 3	Spl. 1	Spl. 2	Spl. 3
120	0.385	0.377	0.377	0.378	0.379	0.381	0.554	0.539	0.542
100	0.448	0.445	0.428	0.383	0.376	0.388	0.54	0.541	0.545
80	0.501	0.491	0.478	0.417	0.403	0.42	0.622	0.608	0.598
60	0.507	0.522	0.505	0.425	0.41	0.408	0.618	0.616	0.587

Table 5. Average Mutual Information for selected sequences in the CC body.

TE	Case A			Case B			Case C		
	Genu 1	Body 2	Body 3	Body 1	Body 2	Spl. 3	Body 1	Body 2	Body 3
120	0.426	0.427	0.416	0.409	0.391	0.382	0.609	0.599	0.615
100	0.477	0.453	0.481	0.428	0.397	0.403	0.577	0.563	0.581
80	0.561	0.553	0.542	0.453	0.42	0.433	0.663	0.652	0.674
60	0.604	0.589	0.578	0.45	0.418	0.425	0.716	0.698	0.71

Table 6. Average Mutual Information for selected sequences in the CC genu.

TE	Case A			Case B			Case C		
	Genu 1	Genu 2	Genu 3	Genu 1	Genu 2	Genu 3	Genu 1	Genu 2	Genu 3
120	0.392	0.355	0.361	0.395	0.341	0.387	0.594	0.548	0.564
100	0.424	0.387	0.396	0.39	0.339	0.43	0.553	0.528	0.539
80	0.484	0.45	0.447	0.42	0.394	0.385	0.639	0.587	0.582
60	0.505	0.476	0.498	0.383	0.362	0.392	0.613	0.589	0.625

These results do not necessary signify that lesser performing sequences are unable to capture anatomical properties, rather that they are unsuitable to observe the relative change. A visual interpretation can be made by comparing changes in MD, AD, RD, and FA between an optimized sequence, and a poorly performing sequence. Fig. 4.5 and Fig. 4.6 show the change in DTI metrics at progressive stages of demyelination across all models and CC regions. When the myelin is fully developed the recorded AD is much higher than the radial and mean diffusivities, signifying that the diffusion is mainly confined to a single axial direction. As the width of myelin decreases the extra-axonal space increases giving the particles more free range to diffuse thereby reducing the directionality of movement and making the diffusion more isotropic (or less anisotropic). This effect is highlighted by a decrease in FA. The increasing in RD demonstrates a rise in particle movement in non-axial directions which also leads to a small rise in MD. The simulations don't record any significant variations in AD as it tends to be variable in white

matter changes and pathology. The results also demonstrate that at a healthy state, MD and RD values are slightly higher for the body, whereas FA values are highest for the splenium, confirming observations recorded in the literature [134].

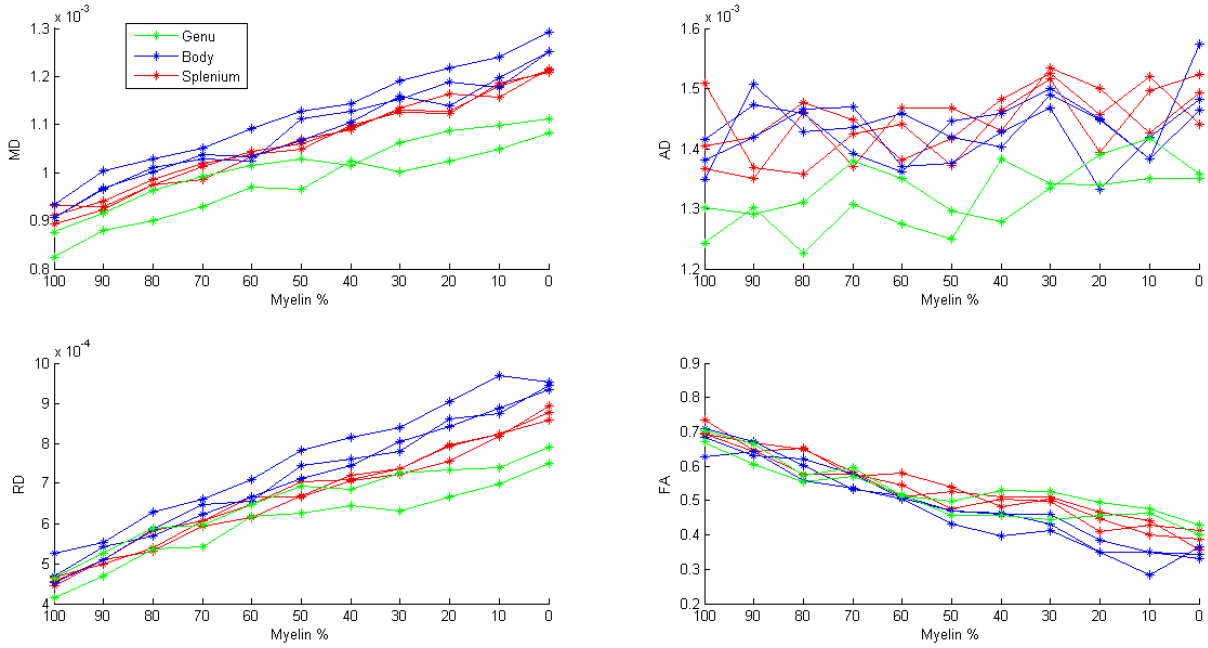

Fig. 4.5: DTI metrics for optimized sequence (TE = 100ms, δ = 19ms, Δ = 56ms)

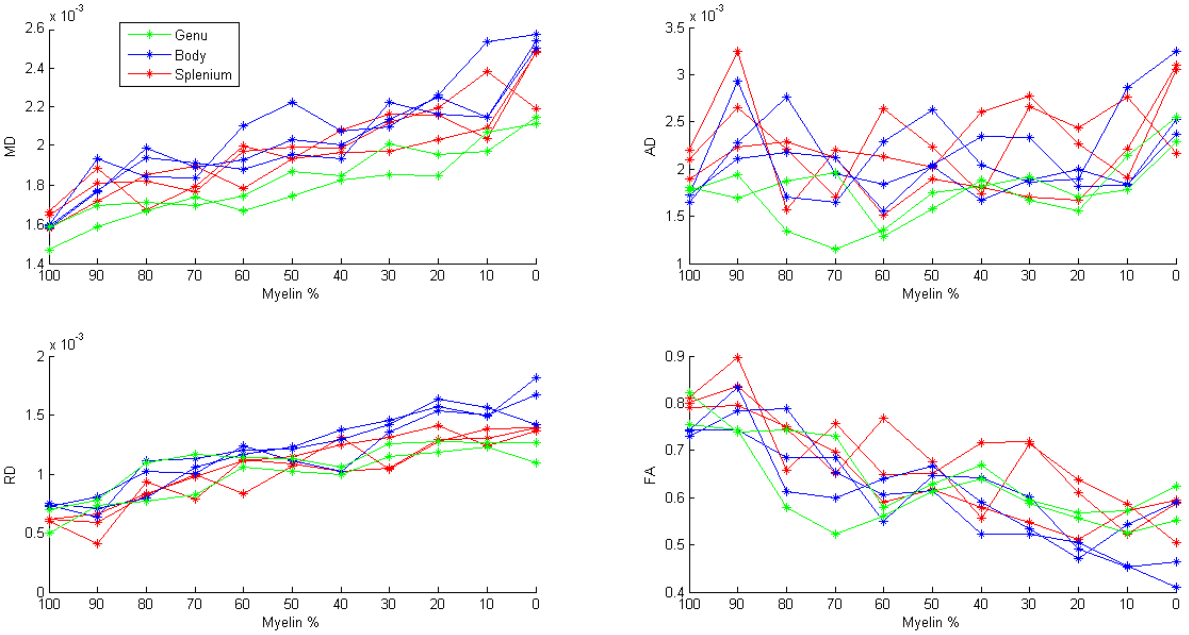

Fig. 4.6: DTI metrics for a non-optimal sequence (TE = 80ms, δ = 31ms, Δ = 44ms)

The non-optimal sequence (Fig. 4.6) clearly shows that it cannot adequately determine the change in DTI metrics, and sometimes indicates a contradicting increase in FA or decrease in MR or RD. On the other hand the chosen optimal sequence has smooth curves showing steady decreasing FA and increasing MD and RD. This may be due to the fact that the non-optimal sequence also over-estimates diffusivity measures. It is worth mentioning that the simulated demyelination process does not correspond to a specific timeline in real subjects. This effect can be recorded over a few days, as in the case of an acute MS flare-up or brain injury, or potentially several months or years in the case of longitudinal MS and chemotherapy studies. In the latter case axon formations may substantially change and reorder even in the same ROI which is not represented in this simulation.

4.4.2 Compartmental Analysis

The results showed thus far result from the combined diffusions from all water compartments. A compartmental analysis of data from a splenium model acquired using the optimized sequence (TE = 100ms, δ = 19ms, Δ = 56ms) reveals how the demyelination effect is mainly driven by the extra-axonal water while the other compartments are unchanged (Fig. 4.7). At full demyelination, the external particles exhibit an almost complete isotropic diffusion with measured FA at 0.2. As expected the directional diffusion is from the intra-axonal particles, with the highest AD and the lowest RD that remain near constant throughout the simulation. A small decrease in myelin diffusivity is observed but this may be explained by a reduction in myelin signal intensity instead of an actual change in diffusion. As the myelin thickness reduces the number of particles contained inside is transferred to the extra-axonal compartment reducing the sample size of myelin particles. Note that at 0% the myelin signal is unavailable since no myelin particles are present.

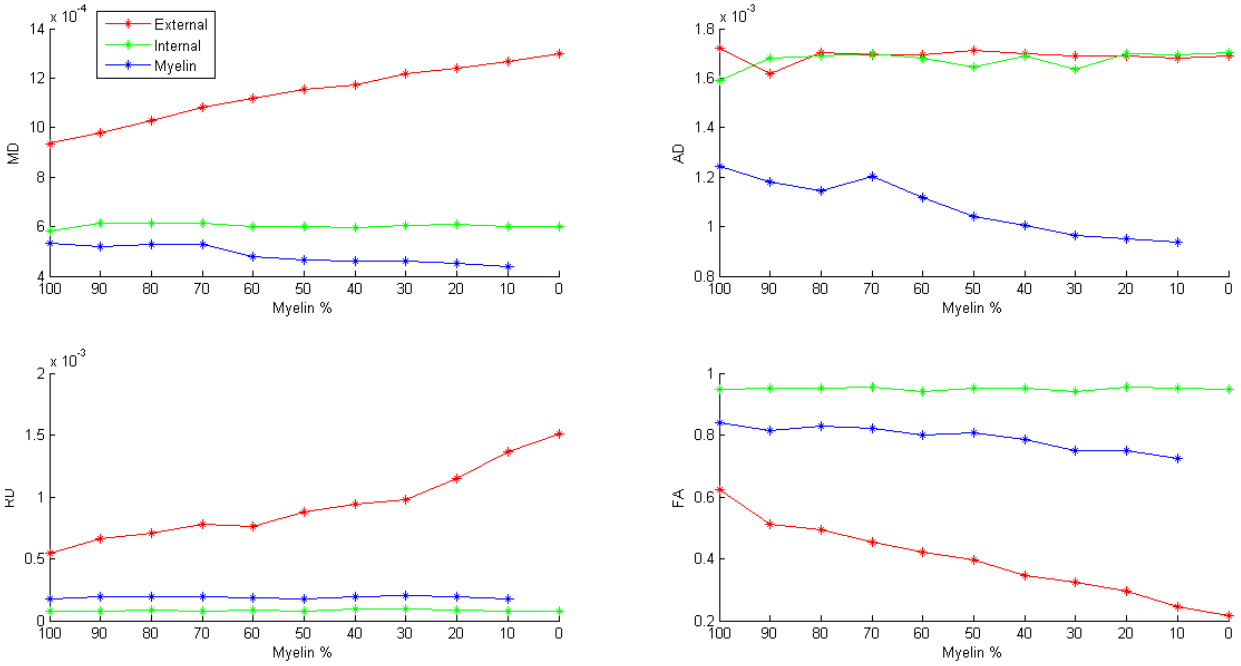

Fig. 4.7: DTI metrics for each water compartment.

4.4.3 Effect of SNR and b-Value

Additional simulations are performed to observe the effect of low SNR and modifying the b-value. In each case the same experiment is executed on five different models of the CC body using a PGSE acquisition sequence with timing TE = 120ms, δ = 18.9ms, and Δ = 50ms.

For the b-value, timing parameters δ and Δ are fixed such that the change in b depends only on the gradient strength g from (13). Results in Fig. 4.8 show that lower b-values tend to overestimate the diffusivities, but do not seem to affect the FA for all stages of demyelination. With the case of noise, ground-truth noiseless data is compared with acquisitions at different levels of SNR. Results in Fig. 4.9 show a contrast to b-value, where average diffusivity measures are generally not affected, except for an increase in uncertainty for lower SNR. However FA measures are slightly overestimated with low SNR acquisitions, confirming this observation

made in several studies. Yet this only occurs for healthy subjects (myelin > 70%) and appears to be more arbitrary as demyelination increases.

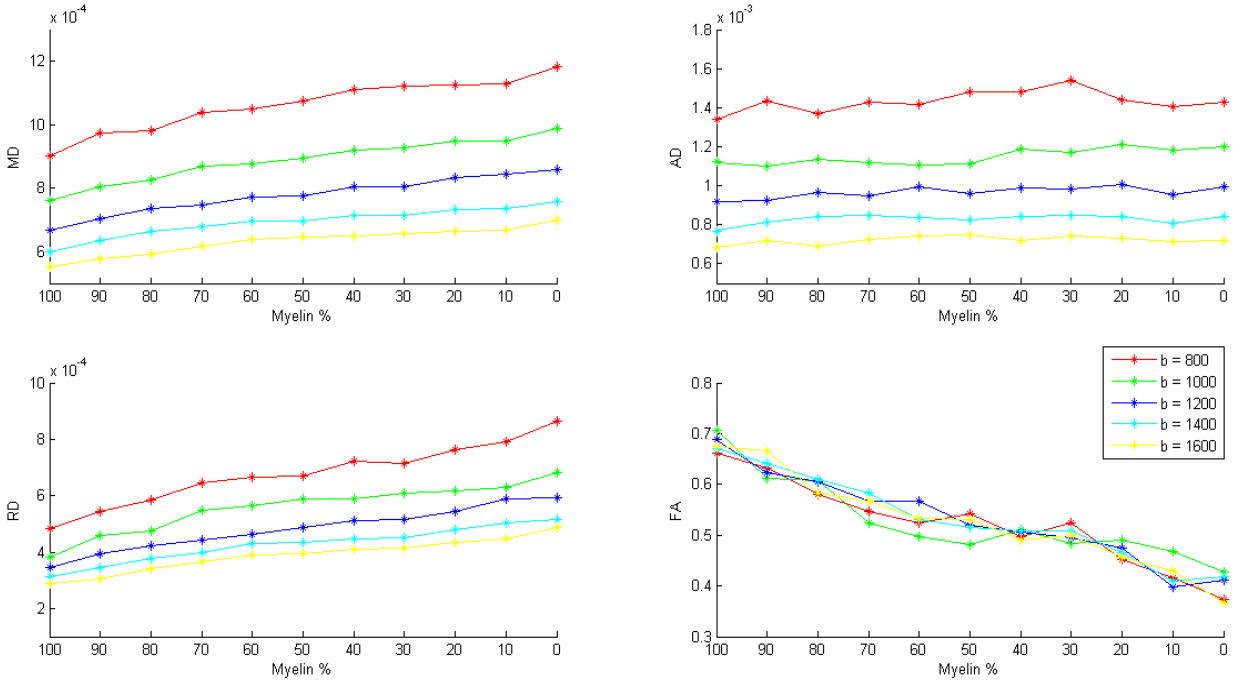

Fig. 4.8: DTI metrics for different b-values.

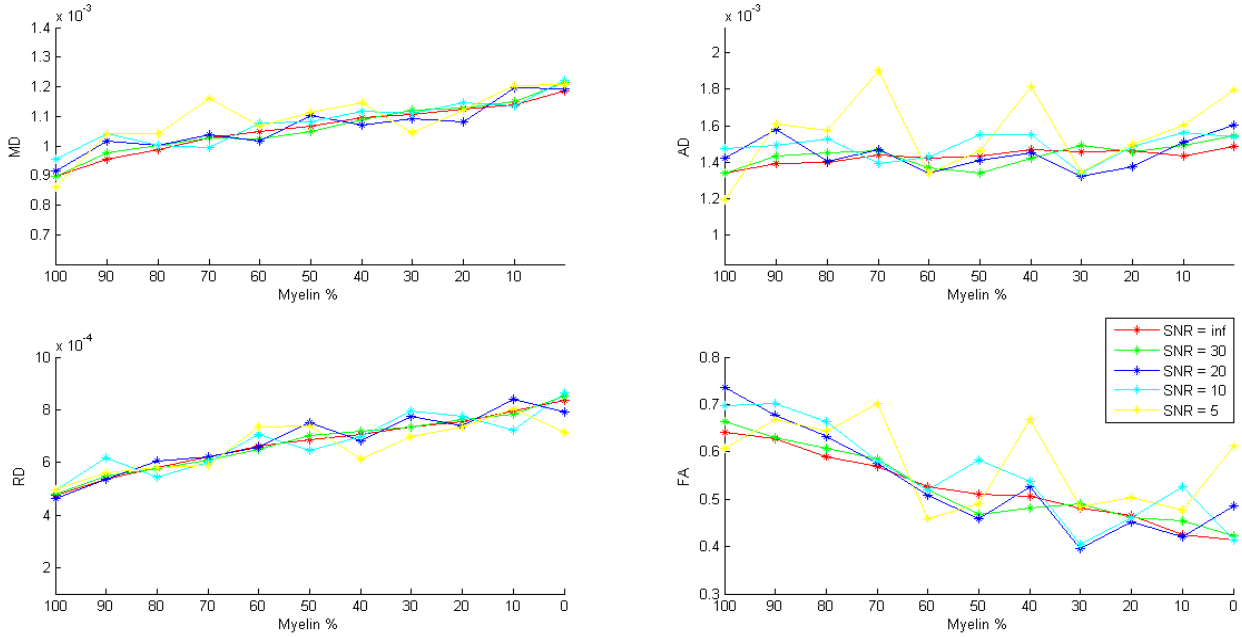

Fig. 4.9: DTI metrics at different levels of SNR.

4.5 Beyond Demyelination

While demyelination has been the most studied phenomenon as it is a common symptom for many brain injuries and abnormalities, gliosis and compaction are much less analyzed and in fact less understood by the medical community. Gliosis usually accompanies demyelination, but it is not always the case depending on what initiated the process. In some cases such as MS flares, demyelination is accompanied by gliosis quickly followed by a partial remyelination. However in many cases of chemotherapy no gliosis is observed since the formation of glia progenitor cells is blocked. And in some studies [120] it has been hypothesized that a long term effect of chemotherapy, where remyelination does not occur, is a reduction in total brain volume such that axons become more compact in order refill extra-axonal volume.

In this section various cases of demyeliation, gliosis, and compaction are simulated to observe and characterize their respective effects on DTI metrics. Four cases are studied, (i) total demyelination without gliosis or compaction as performed in the previous sections, (ii) demyelination with gliosis, (iii) demyelination with gliosis followed by partial remyelination, and (iv) total demyelination without gliosis followed by axon compaction. In the following simulations, demyelination occurs sequentially as outlined in the previous experiments from 100% to 0%; gliosis happens as a response to demyelination in two stages, the number of glia doubles first at 50% demyelination then at 20%; remylination is in turn a response to gliosis starting at 20% and reverses the trend by increasing myelin thickness. In the final case axon compaction takes place at a later stage extending beyond demyelination. As pointed earlier these events do not necessarily correspond to a specific timeline or happen in the order presented herein. Each case is simulated on a model of the CC body, and data acquisition is performed with a PGSE sequence with timings TE = 120ms, δ = 18.9ms, Δ = 50ms, and b = 1200s/mm^2 and

SNR at 30db. Results are reported in Fig. 4.10. From 100% to 50% myelin, all cases follow the same trend. Demyelination with and without gliosis highlighted by the red and green curves respectively are hardly discernable from one another indicating that gliosis does affect FA and diffusivity measures. Conversely the dark blue curve showing gliosis followed by a partial remyelination starting at 20% stopped the increase in MD and RD and slowly reversed the drop in FA. In the final case, axon compaction also reverses the observed trend with a sharp increase in FA and AD, and a drop in MD and RD with values comparable to remyelination.

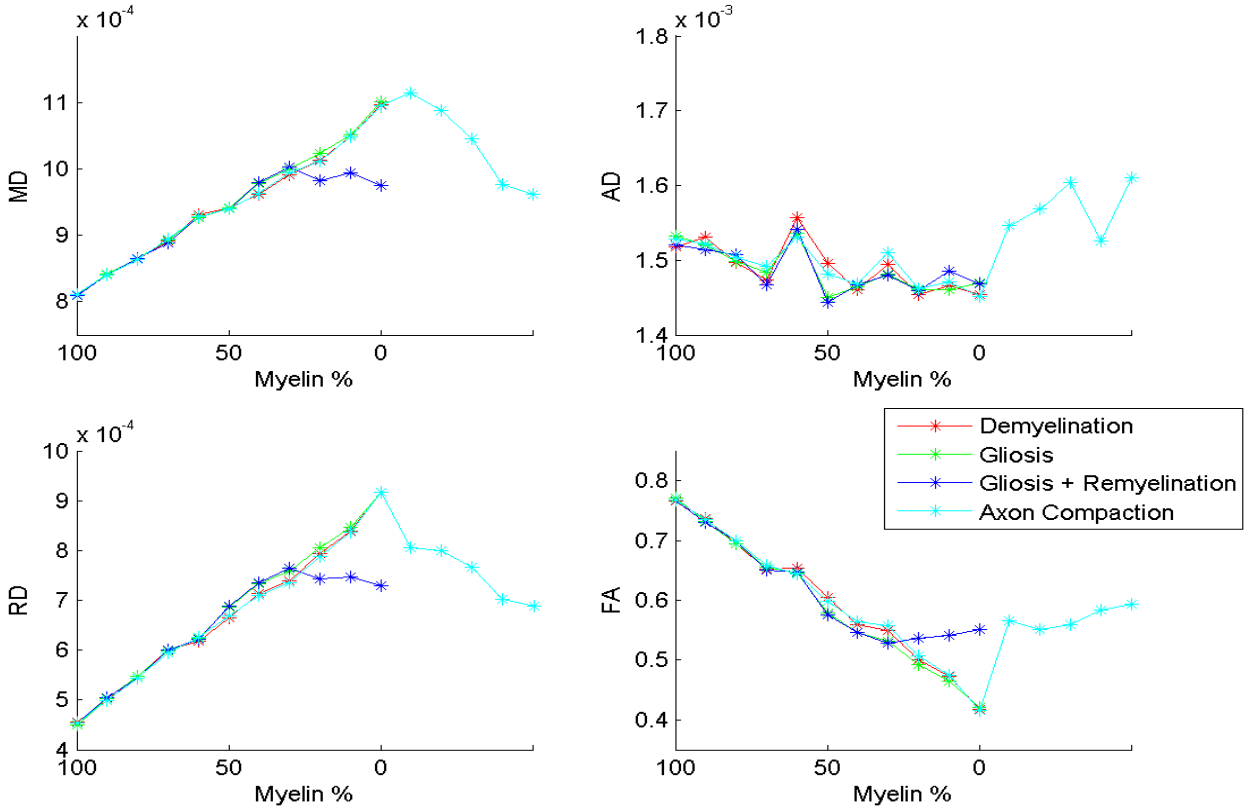

Fig. 4.10: DTI metrics for demyelination, gliosis, remyelination, and axon compaction.

4.6 Interpretation and Significance

The experiments above confirm that not all acquisition sequences are capable of correctly capturing demyelination. Fig. 4.5 demonstrates how optimized sequences can strongly

decorrelate the change in FA and diffusivity measures, signaling a loss of myelin, whereas non-optimal sequences in Fig. 4.6 cannot capture those changes. Another observation is that the best performing sequences use shorter gradients pulses δ. This suggests that variations in myelin thickness have more localized effects on particle diffusion. To understand this, consider the hypothetical path of a diffusing extra-axonal particle illustrated in Fig. 4.11. The shorter pulse δ_1 records a shorter absolute distance traveled when compared with the longer pulse δ_2. This divergence in diffusivity measures is marked when comparing the optimal sequence (Fig. 4.5) with a non-optimal sequence (Fig. 4.6). Non-optimal sequences use longer pulses and diffusion times, which accounts for the higher recorded MD values driven by a higher AD and RD. As the myelin shrinks, the change in diffusion patterns is more pronounced when measuring distance over short durations.

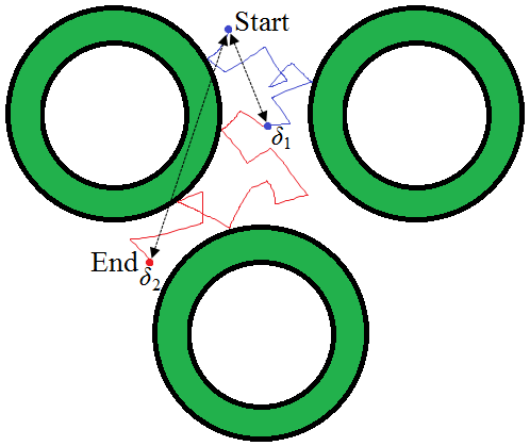

Fig. 4.11: Hypothetical diffusion path of an extra-axonal particle between myelinated axons, and the absolute measured distance with short and long gradient pulses δ_1 and δ_2 respectively.

The final experiment comparing the influence of gliosis and compaction confirm that gliosis has no influence on DTI measurements. On the other hand, a white matter compaction of axons results in similar measures to a partial remyelination. In a study on survivors of childhood acute

lymphoblastic leukaemia, Edelmann et. al. [120] recorded increases in FA among subjects treated with chemotherapy accompanied by a reduction in WM volume. While increasing FA may suggest compensatory remyelination, survivors demonstrated significant long term deficiencies in neurocognitive functions refuting this argument. The proposed conjecture is that this was due to a compaction of axons in WM which may exhibits similar signs to remyelination. The results reported in this chapter validate those findings.

V. MULTI-TENSOR MODELS TO RESOLVE COMPLEX STRUCTURES

Limitations with the tensor model to represent the true orientation of fibers have been exposed early. The main objection is that a tensor can only express motion in three directions, whereas multiple bundles within a voxel can have many more. This chapter examines some of the most common alternative methods proposed to resolve this issue. In particular the models put to test are, Q-ball imaging analyzed with high angular resolution diffusion imaging (HARDI) data, spherical deconvolution (SD), and the composite hindered and restricted model of diffusion (CHARMED). The main contribution is that FiberBlender can produce ground-truth directional tensors that can be used as a basis for the evaluation of each model. The chapter begins with a structural description of crossing fiber models, their characteristics and location in the brain, followed by a review of diffusion models and their relevant equations, and finally provides a comparative performance result for each method.

5.1 Crossing Fibers

The issue of multi-tensor models most often comes when analyzing voxels with crossing fibers which, unlike the CC, are prevalent in the brain. These are most often seen when studying nerve connections in the frontal lobe and pyramidal tracts (Fig. 5.1) where single diffusion tensor based methods most often fail due to the complexity of fiber intersections [135]. These regions are essential to all cognitive studies as the frontal lobe controls important skills such as emotional expression, problem solving, memory, and language, while the pyramidal tracts are responsible for motor functions and muscle movement as they conducts nerve impulses from the center of the brain to the spinal cord. Multiple studies on human subjects [135 - 139] found that axon diameters in cortical white matter ranged from 0.3 to 9μm generally following a gamma

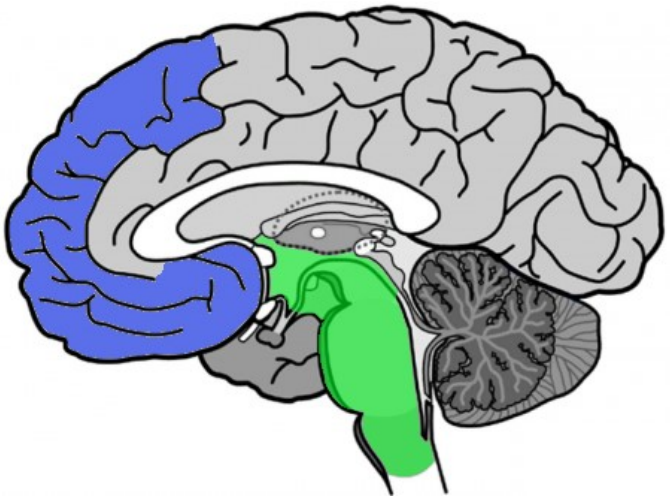

Figure 5.1: Midsagittal view of the brain with highlighted locations of the frontal lobe (blue) and pyramidal tracts (green).

distribution. The pyramidal tracts contain the largest regional variations with axons well over 5μm with relatively large g-ratios (> 0.7), often found in proximity or crossing with significantly smaller fibers (< 1μm) with a g-ratio scattered broadly around 0.6. In the frontal lobe axons are considerably smaller with average diameters between 0.5 and 0.9μm whereas the g-ratio is much higher than other regions (~0.8). While these measurements are not necessarily representative of every human brain, they are used to form FiberBlender crossing models. There is little ex-vivo and in-vivo histology data available in the literature for the measurement of regional glia density but it is generally considered to be lower than in the CC. Thus GNR is set at 2.5:1. In this chapter, the study will focus on 4 types of models representing four different cases of crossing fibers. The first three contain small axons (< 2μm average diameter) crossing at different angles of 30˚, 60˚and 90˚respectively (Fig. 5.2). The fourth model contains axons crossing at 60˚but with a difference in size such that in one direction the same small axons from the first three

models are used, while in the second direction the average diameter is increased to 6μm. All models are formed as isotropic voxels with a fixed size of 120×120×120μm, to remove any bias.

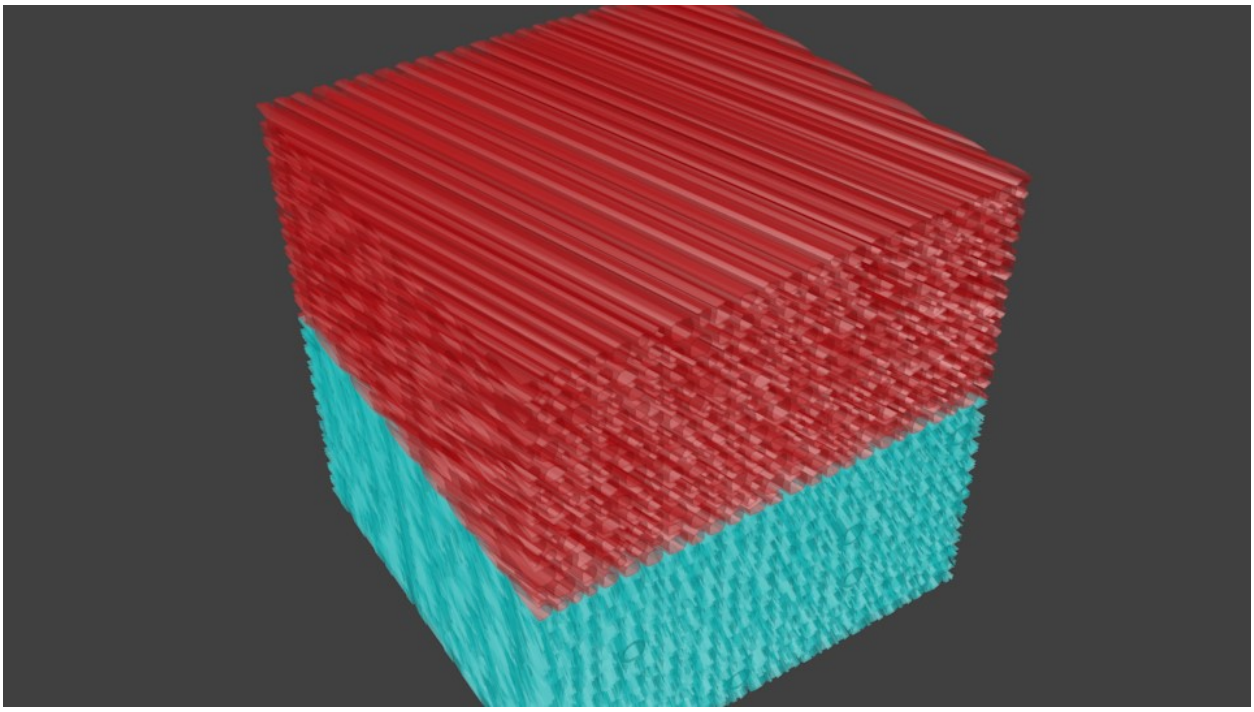

Figure 5.2: Example of a crossing model at a 30° angle.

5.2 Multi-Tensor Models

The main approach to resolving crossing fibers is to represent the diffusion not only by a single tensor, but as a mixture of multiple tensors, each characterizing a different fiber population. This results in the signal S originally calculated from (12), now being obtained as a linear combination of multiple tensors such that,

$$S = \sum S_i e^{-D_i b}. \tag{35}$$

The first successful results were introduced by Tuch [140] with the high angular resolution diffusion imaging (HARDI) model which in essence consists of measuring the diffusion signal using a much larger number of uniformly distributed gradient directions than required for DTI to

capture the higher angular frequency features of the signal that are not adequately modelled by a single diffusion tensor. The problem then becomes one of fitting multiple tensors to recover the fiber orientations that best explain the measured signal. The solution proposed in [140] using a mixture model decomposition of the signal suffered from a large number of parameters to fit the model that are prone to overfitting and require long computation times. Yet the HARDI signal acquisition process that specifies the number and directions of diffusion gradients became standard protocol for many multi-tensor models.

Then, multiple models have been proposed for the analysis of HARDI data, first by Tuch himself who introduced Q-ball imaging [141]. Q-ball employs the q-space method originally proposed by Callaghan [142], where no specific model of water diffusion is originally assumed. Instead the signal attenuation profile is calculated with respect to q ($q = \gamma\delta g/2\pi$). In this way diffusivity measures do not use ADC modeling, but are based on the estimation of the probability density function of the average spin displacement of water molecules. Another popular approach based on q-space is CHARMED introduced by Assaf et. al. [143]. This approach relies on measuring the signal as a combination from different water compartments, each extracted as a non-linear least squares model fitting. Tournier et. al. [144] proposed spherical deconvolution (SD) as an alternative to calculate a fiber orientation distribution. This is based on the concept that the distribution of diffusion signals can be represented by fiber orientation distribution convoluted with its signal response. SD is one of the best approaches to achieve high angular resolution analysis, and doesn't require model fitting.

Each of these methods is popular and extensively used by researchers in the DTI community with their implementations offered in free and publicly available DTI analysis and reconstruction software such as FSL, DTI-studio, DTI-toolkit, and CAMINO. However these programs are

designed to work with direct MRI raw data files produced from scanners in NifTI format. In FiberBlender, the system produces text files representing the coordinates of particles which are used to calculate displacement vectors, phases, and so on. Therefore in this work Q-ball, SD and CHARMED are re-implemented with MATLAB to process HARDI diffusion data obtained with FiberBlender. CHARMED is implemented using in-house software, while the implementation of Q-ball and SD is based in part on publicly available software provided from [145].

5.2.1 Q-ball

Tuch's method aims at reconstructing the orientation distribution function (ODF) of a fiber population that characterizes the relative likelihood of water diffusion along any given angular direction $\mathbf{u}$. Because both the ODF and the diffusion signal are defined on a spherical domain, it is convenient to normalize spherical points to unit magnitude and adopt a spherical coordinate system $\mathbf{u}(\theta, \phi)$, where θ and ϕ denote elevation and azimuth respectively. Similar to the Fourier transform used to decompose images, this approach uses spherical harmonics (SH) as a way to decompose signals on the sphere. The implementation in this work is based on a simplification of the original method found in [146]. To obtain the values of the q-ball ODF at desired points, the acquired data is used to expand the diffusion signal $E(\mathbf{u}) = S(\mathbf{u})/S_0$, over an order L harmonic representation

$$E(\mathbf{u}) = \sum_{l=0}^{L} \sum_{m=-l}^{l} 2\pi c_l^m Y_l^m(\mathbf{u}) \tag{36}$$

where $Y_l^m(\mathbf{u})$ denotes spherical harmonics with order l and phase factor m, and c_l^m denotes the harmonic series coefficients.

5.2.2 CHARMED

The CHARMED framework includes hindered and restricted compartments, allowing for N distinct fiber populations such that

$$E(q,\Delta) = f_h \cdot E_h(q,\Delta) + \sum_{j=1}^{N} f_r^j \cdot E_r^j(q,\Delta). \tag{37}$$

where $E(q,\Delta)$ is the measured signal decay, f_h and $E_h(q,\Delta)$ are the relaxation-weighted volume fraction and signal decay of the hindered part respectively, whereas f_r and $E_r(q,\Delta)$ are the relaxation-weighted volume fraction and signal decay of the restricted part respectively. The experimental data is fit to the model with a non-linear least-square estimation procedure utilizing Levenberg–Marquardt minimization. In the case of two directions of crossing fibers three signal decays are considered, one for the hindered compartment representing the extra-axonal space and two for the restricted compartments, $N = 2$ in (36), of the intra-axonal space and myelin.

5.2.3 Spherical Deconvolution

SD methods have become very popular due to the fact that, as opposed to model-free techniques that estimate the diffusion ODF such as Q-ball, the output from SD is directly the fiber ODF itself. Similar to CHARMED the signal is a expressed as a linear combination from several water compartments.

$$S = S_0 \cdot \sum_{i=1}^{M} f_i exp(-b_i g_i^T \mathbf{D}_i g_i) \tag{38}$$

where M is the number of WM parallel fiber bundles, f_i denotes the volume fraction of the i-th fiber bundle compartment so that $\sum_{i=1}^{M} f_i = 1$. In this formulation, $\mathbf{D}_i$ denotes the anisotropic diffusion tensor of the j th fiber-bundle such that $\mathbf{D}_i = \mathbf{R}_i^T \mathbf{A} \mathbf{R}_i$ where $\mathbf{R}_i$ is the rotation matrix that rotates a unit vector initially oriented along the x axis toward the i-th orientation (θ_i, ϕ_i) and

A is a diagonal matrix containing information about the magnitude and anisotropy of the diffusion process inside that compartment

$$\mathbf{A} = \begin{bmatrix} \lambda_1 & 0 & 0 \\ 0 & \lambda_2 & 0 \\ 0 & 0 & \lambda_3 \end{bmatrix}. \tag{39}$$

The measured signal in (38) can be re-evaluated in matrix form as

$$\mathbf{S} = \mathbf{Hf}, \tag{40}$$

such that $\mathbf{H}_{ij} = S_0.exp(-b_i g_i^T \mathbf{D}_j g_i)$ is an $N \times M$ matrix where every column of length N contains the signal in (38) for a single fiber-bundle compartment oriented along one of the M directions, and **f** the fiber ODF represented as a set of basis functions on the unit sphere. Solving the deconvolution problem given in (40) results in an ill-conditioned and ill-posed system of linear equations. Common algorithms to avoid such instabilities estimate the fiber ODF by constraining it to be non-negative and symmetric around the origin. In this study the Richardson-Lucy algorithm is used [147].

5.3 Results

Four simulations are performed, the first three to measure crossing at different angles, and the fourth compares crossing of differently sized fibers. In the first case all axons are generated following a gamma diameter distribution with mean 1μm, g-ratio is set at 0.8 and GNR at 2.5:1. In the final case the same parameters are used for the direction with small fibers, while the direction with larger fibers contains gamma distributed axons with mean 6μm, g-ratio 0.65 and similar GNR at 2.5:1. All voxels are120×120×120μm simulated with 50,000 particles diffusing at a rate of D = 2.6mm^2/s for intra and extra-axonal, and D = 2.6mm^2/s for myelin particles. Data is acquired with a PGSE sequences using a uniform HARDI sampling scheme with 60 directions.

Sequence parameters are different for each method and are chosen based on values used in published studies [71, 141, 143, and 146]. One difference with [141] is that Tuch uses a twice refocusing spin echo (TRSE) acquisition sequence which can be thought of as a double PGSE with two periods, generally used to minimize Eddy current induced distortions. Single shell acquisition is performed with constant b-value at b = 1200s/mm^2 and timing parameters as reported in table 8.

Table 8. Sequence parameters for crossing fiber analysis.

Timing parameter (in ms)	FiberBlender	Q-ball	CHARMED	SD
TE	100	120	200	120
Δ	60	60	150	100
δ	20	55	40	5

The goal of this experiment is to find which method best describes the true directionality of the crossing fibers and the relative diffusivity in each direction. Data is acquired at high and low SNR (25db and 4db) with results in Fig. 5.3 and Fig. 5.4 respectively.

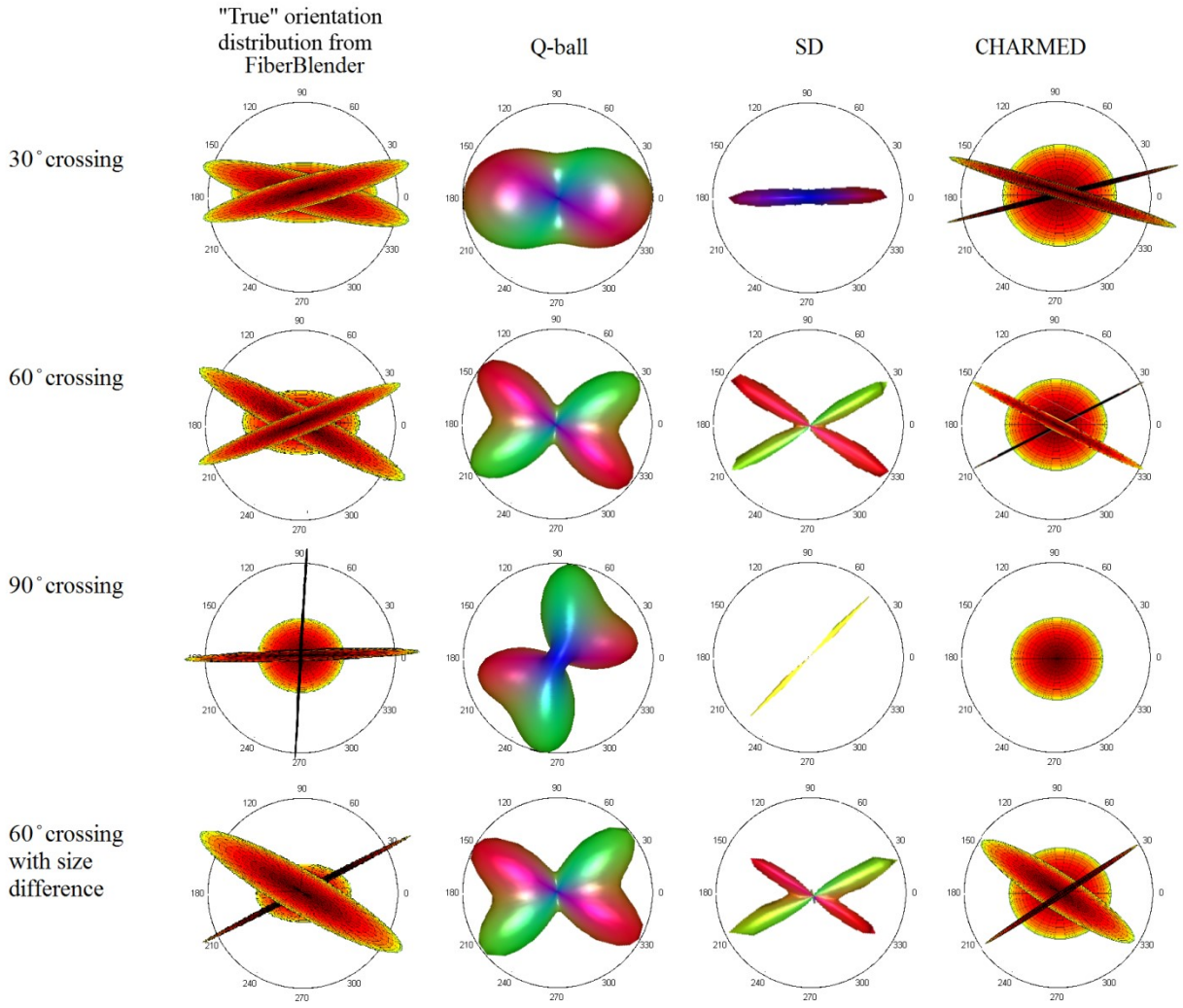

Fig. 5.3: Comparison of fiber crossing algorithm at SNR = 25.

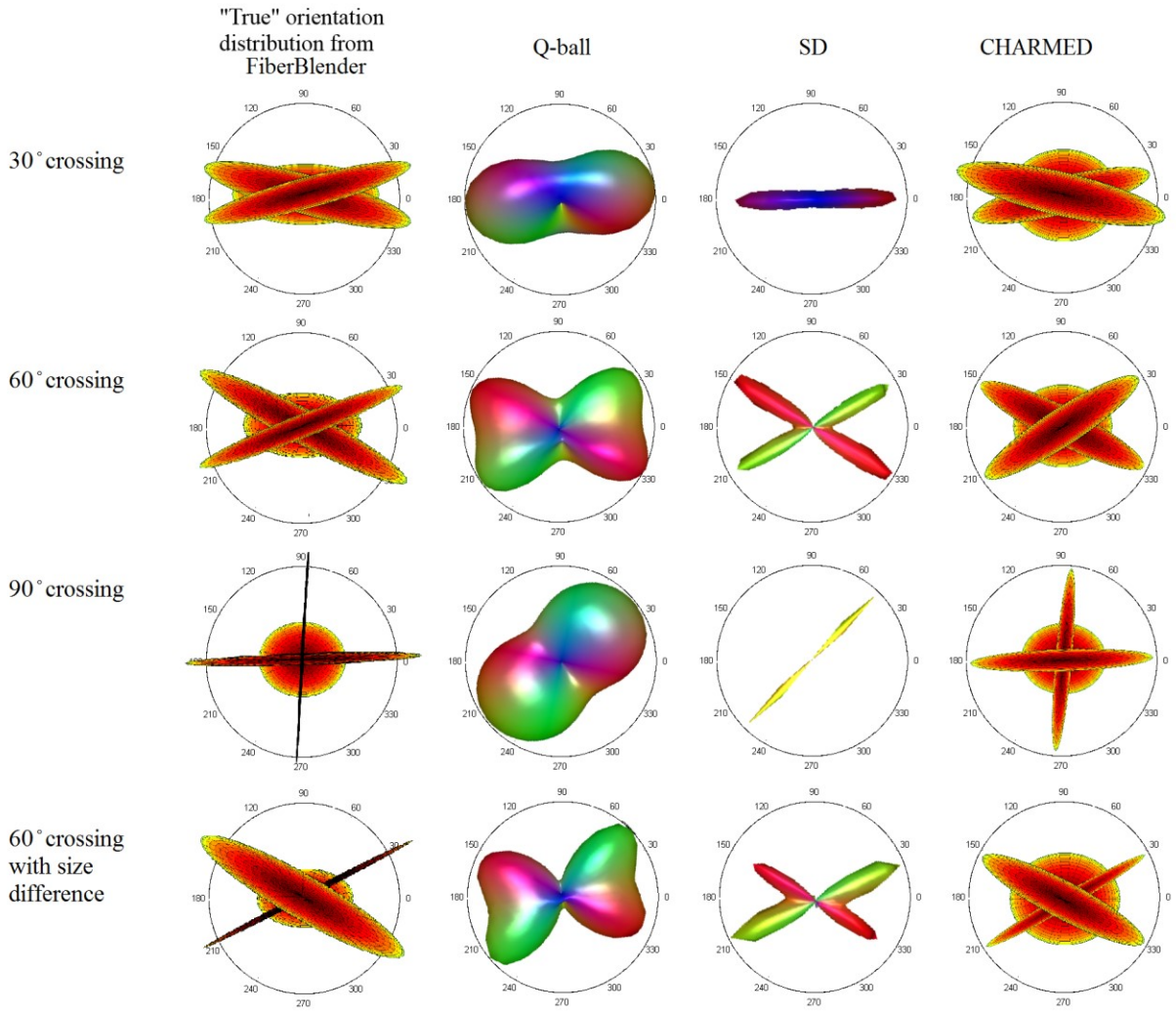

Fig. 5.4: Comparison of fiber crossing algorithm at SNR = 4.

The first columns in Fig. 5.3 and 5.4 represent the ground-truth fiber orientations obtained with blender for separate water compartments (extra-axonal vs. intra-axonal and myelin). While this serves as a basis for comparison, these tensors are still prone to error since they rely on the accuracy of data generated with Blender. Three tensors are represented: one tensor for the hindered diffusion of extra-axonal particles, and two tensors for the restricted diffusion of particles in each of the two directions. When the crossing angle is low, the hindered tensor still maintains some directionality, but becomes steadily more isotropic as the crossing gets more perpendicular. Most of the orientation information comes from the restricted diffusion

The following columns represent the fiber orientations estimated with Q-ball, spherical deconvolution, and CHARMED algorithms respectively. Results suggest that Q-ball and SD do not perform well for crossings at a low angle of 30° making the diffusion look almost confined to a single direction. The inability to resolve this may be due to the relatively small number of gradient directions used. Some studies use over 100 directions to get a better approximation making the simulation much more computationally demanding, or requiring longer scans to obtain clinical data. All methods perform well at 60° where the difference in direction is more pronounced for both cases of crossing fibers with similar size and variable size. In the case of different diameters, the tensor produced by the smaller axons is much more anisotropic than with larger axons signaling a difference in FA values between the two directions.

This high directionality is also observed when the fibers are perpendicular. This does not necessarily mean that absolute diffusivities are higher, but simply that the differences between hindered and restricted diffusivities are greater. For 90° SD was unable of resolving the correct fiber orientations. Although Tournier [73] observed a bias with SD for fibers with 90° crossings, it should still be capable of differentiating the orientation, and these results are not supported

anywhere in the literature. A more comprehensive study would need to be performed comparing Richardson-Lucy deconvolution with different SD algorithms including Tournier's constrained spherical deconvolution method to determine the source of this error.

In this study CHARMED is arguably the best performing approach for all crossing cases since it is based on both hindered and restricted compartment modeling, and the tensors most closely match those of FiberBlender. One noticeable difference is that the hindered tensor is near spherical for all cases and doesn't capture any directionality and in the case of low SNR (Fig. 5.4) the restricted diffusivities are under estimates. Most of these methods perform poorly with lower SNR with the exception of 60° crossing angle. While SNR is an important factor in direction estimation, another element is the size of the voxel. All the simulations have been performed on 120×120×120μm voxel that are in reality much smaller than actual scanner resolutions. Therefore it is not clear how these results can be extrapolated to larger voxels and further studies will be required with larger models to examine the influence of voxel resolution.

VI. CONCLUSIONS AND FUTURE RESEARCH

6.1 Contributions

The main contributions of this work are detailed in chapters 3, 4, and 5. Chapter 3 introduces FiberBlender and all of its components as a novel DTI modeling and simulation system. This tool can be used to generate fiber bundles in potentially any desired configuration to mimic different regions of the brain. FiberBlender's novelty is in its capability to reproduce brain-like fibers with high accuracy to capture the tortuosity of the axonal space such that axons are randomly placed in the simulation space while still accounting for correct diameter distribution and compactness of the axon structure. The problem of packing cylindrical axons in a cubic volume is approached using both manual operations and computer algorithms. The myelin sheath and glial cells are also represented with controllable size and density ratios respectively. With this framework FiberBlender can produce multiple models representing the regional contrasts between different brain regions as well as the contrast among human subjects. This is necessary to validate and optimize acquisitions schemes across multiple test subjects. Another innovation with this system is its ability to tune geometries in order to simulate axon and myelin damage; in particular the cases of demyelination, gliosis and axon compaction.

Chapter 4 performs a study of these conditions with the aim of finding an optimized acquisition scheme that is best suited to capture the effect of demyelination on the observed DTI measurements. Since demyelination, gliosis and compaction result in a change in diffusivity, the innovative optimization process aims at finding the sequence that minimizes the mutual information obtained from an acquisition. Results suggest that PGSE sequences with short pulses δ and longer diffusion times Δ are the most valid. Optimized sequences are then used to examine the influence of noise and b-level values on demyelination measurements. The choice of b-value

heavily influences the measured diffusivity while keeping FA relatively constant; conversely SNR biases FA measurements. Lastly a comparative study of demyelination, gliosis and compaction suggested that gliosis does not affect the DTI signal, while axon compaction exhibits comparable measurements to a partial remyelination. This finding may confirm observations in cancer survivors who appeared to show signs of remyelination that did not correspond with any improvement in cognitive performance. This suggests that axon compaction is the more likely hypothesis.

Finally in chapter 5, a comparison of the most widely used multi-tensor models is performed on CHARMED, SD, and Q-ball methods. The accuracy of each model is validated against ground-truth tensor data generated with FiberBlender. Preliminary results point to CHARMED as the most reliable method. Further investigation is needed to understand the effect of voxel size and why SD does not perform well in some cases.

6.2 Future Work

In the future, the FiberBlender system can be extended in one of two ways. The first improvement would be to produce much larger models to approximate real scanner dimensions with the potential of creating multiple sub-voxels. This enhancement would allow the study of crossing fiber not only for a single voxel but across an ROI with the possibility to perform tractography studies. In addition to crossing, other fiber configuration may be considered. Most notably, bending and Y-shaped, with a single multi-voxel model containing a mixture of fiber orientations could be investigated.

Another approach is to go deeper in the study of myelin. Myelin water diffusion imaging is a recently proposed DTI approach with the potential of differentiating the myelin signal from other

water compartments and produce DTI images from myelin water only. In this context FiberBlender can be used to simulate and validate myelin specific acquisition sequences.

Lastly, while Blender has proven to be a great tool for modeling axon structure, other simulation systems can be considered as an alternative, especially when simulating much larger volumes. Although Blender rendering uses CUDA for GPU powered parallel computing, physics and motion calculation as performed in this system is only GPU powered. Since Blender objects can be exported to other systems, the new framework can still use it for generating axon structure as detailed in this work but the particle diffusion simulation would be performed with another tool.

REFERENCES

[1] F. A. Howe, A. G. Filler, B. A. Bell, and J. R. Griffiths, "Magnetic resonance neurography," *Magnetic Resonance in Medicine*, vol. 28, no. 2, pp. 328–338, December 1992.

[2] P. Basser, S. Pajevic, C. Pierpaoli, J. Duda, and A. Aldroubi, "In vivo fiber tractography using DT-MRI data," *Magnetic Resonance in Medicine*, vol. 44, pp. 625–632, October 2000.

[3] J. D. Power, A. L. Cohen, S. M. Nelson, G. S. Wig, K. A. Barnes, J. A. Church, A. C. Vogel, T. O. Laumann, F. M. Miezin, B. L. Schlaggar, and S. E. Petersen, "Functional network organization of the human brain," *Neuron*, vol. 72, no. 4, pp. 665–678, November 2011.

[4] S. Mori and P. B. Barker, "Diffusion Magnetic resonance imaging: its principle and applications," *The Anatomical Record*, vol. 257, pp. 102–109, 1999.

[5] D. Le Bihan, J. F. Mangin, C. Poupon, C. A. Clark, S. Pappata, N. Molko, and H. Chabriat, "Diffusion tensor imaging: concepts and applications," *Journal of Magnetic Resonance Imaging*, vol. 13, no. 4, pp. 534–546, April 2001.

[6] A. L. Alexander, J. E. Lee, M. Lazar, and A. S. Field, "Diffusion Tensor Imaging of the Brain," *Neurotherapeutics*, vol. 4, no. 3, pp. 316–329, July 2007.

[7] J. M. Soares, P. Marques, V. Alves, and N. Sousa, "A hitchhiker's guide to diffusion tensor imaging," *Frontiers in Neuroscience*, vol. 7, no. 31, 2013.

[8] D. K. Jones, "Precision and accuracy in diffusion tensor magnetic resonance imaging," *Topics in Magnetic Resonance Imaging*, vol. 21, no. 2, pp. 87–99, April 2010.

[9] A. Seehaus, A. Roebroeck, M. Bastiani, L. Fonseca, H. Bratzke, N. Lori, A. Vilanova, R. Goebel, and Ralf Galuske, "Histological validation of high-resolution DTI in human post mortem tissue," *Frontiers in Neuroanatomy*, vol. 9, no. 98, July 2015.

[10] A. S. Choe, I. Stepnewska, D. C. Colvin, Z. Ding, and A. W. Anderson, "Validation of diffusion tensor MRI in the central nervous system using light microscopy: quantitative comparison of fiber properties," *NMR in Biomedicine*, vol. 25, no. 7, pp. 900–908, January 2012.

[11] M. J. Levene, D. A. Dombeck, K. A. Kasischke, R. P. Molloy, and W. W. Webb, "In vivo multiphoton microscopy of deep brain tissue," *Journal of Neurophysiology*, vol. 91, no. 4, pp. 1908–12, April 2004.

[12] M. Choi, J. J. S. Kwok, and S. H. Yun, "In Vivo Fluorescence Microscopy: Lessons From Observing Cell Behavior in Their Native Environment," *Physiology*, vol. 30, no. 1, pp. 40–49, January 2015.

[13] H. U. Dodt, U. Leischner, A. Schierloh, N. Jährling, C. P. Mauch, K. Deininger, J. M. Deussing, M. Eder, W. Zieglgänsberger, and K. Becker, "Ultramicroscopy: three-dimensional visualization of neuronal networks in the whole mouse brain," *Nature Methods*, vol. 4, no. 4, pp. 331–336, April 2007.

[14] L. Shen and Z. Chen, "Critical review of the impact of tortuosity on diffusion," *Chemical Engineering Science*, vol. 62, pp. 3748–3755, March 2007.

[15] K. J. Chang, S. A. Redmond, and J. R. Chan, "Remodeling myelination: implications for mechanisms of neural plasticity," *Nature Neuroscience*, vol. 19, no. 2, pp. 190–197, January 2016.

[16] M. P. Gesellschaft, “Glial cells supply nerve fibres with energy-rich metabolic products,” *ScienceDaily*, 10 May 2012
[17] R. M. Andrei, M. Callieri, M. F. Zini, T. Loni, G. Maraziti, M. C. Pan, and M. Zoppè, “BioBlender: a Software for Intuitive Representation of Surface Properties of Biomolecules,” *BMC Bioinformatics*, vol. 13, no. 4, 2012.
[18] E. Catto, “Fast and simple physics using sequential impulses.” *Proceeding in Games Developer Conference*, 2006.
[19] S. J. Chung and N. Pollard, “Predictable behavior during contact simulation: a comparison of selected physics engines,” *Computer Animation and Virtual Worlds*, vol. 27, no. 3–4, pp. 262–270, May 2016.
[20] M. Tamis, “Comparison between Projected Gauss-Seidel and Sequential Impulse Solvers for Real-Time Physics Simulations”, July 2015. [Online]. Available: http://www.mft-spirit.nl/files/MTamis_PGS_SI_Comparison.pdf
[21] C. Thomas, Q. Ye, M. O. Irfanoglu, P. Modi, K. S. Saleem, D. A. Leopold, and C. Pierpaoli, “Anatomical accuracy of brain connections derived from diffusion MRI tractography is inherently limited” *Proceedings of the National Academy of Sciences*, vol. 111, no. 46, November 2014.
[22] A. Rokem, J. D. Yeatman, F. Pestilli, K. N. Kay, A. Mezer, S. van der Walt, and B. A. Wandell, “Evaluating the Accuracy of Diffusion MRI Models in White Matter,” *PLOS ONE*, vol. 10, no. 9, April 2015.
[23] A. E. Fick, “On Liquid Diffusion,” *Philosophical Magazine and Journal of Science*, vol. 10, pp. 30–39, 1855.
[24] A. Einstein, “Über die von der molekularkinetischen Theorie der Wärme geforderte Bewegung von in ruhenden Flüssigkeiten suspendierten Teilchen,” *Annalen der Physik*, vol. 17, pp. 549–560, 1905.
[25] W. Gerlach and O. Stern, “Das magnetische Moment des Silberatoms,” *Zeitschrift für Physik A Hadrons and Nuclei*, vol. 9, pp. 353–355, 1922.
[26] J. S. Townsend, “A Modern Approach to Quantum Mechanics” McGraw-Hill, 1992.
[27] I. I. Rabi, “Space Quantization in a Gyrating Magnetic Field,” *Physical Review*, vol. 51, pp. 652, 1937.
[28] F. Bloch, “Nuclear Induction,” *Physical Review*, vol. 70, no. 8, October 1946.
[29] N. Bloembergen, E. M. Purcell, and R. V. Pound, “Relaxation effects in nuclear magnetic resonance absorption,” *Physical Review*, vol. 73, no. 7, April 1948.
[30] G. J. Stanisz, E. E. Odrobina, J. Pun, M. Escaravage, S. J. Graham, M. J. Bronskill, and R. M. Henkelman, “T1, T2 Relaxation and Magnetization Transfer in Tissue at 3T,” *Magnetic Resonance in Medicine*, vol. 54, no. 3, pp. 507–512, September 2005.
[31] E. L. Hahn, “Spin Echoes,” *Physical Review*, vol. 80, no. 4, April 1948
[32] E. L. Hahn, “Free Nuclear Induction.” *Physics Today*, vol. 6, no. 11, pp. 4, 1953.
[33] H. Carr, “Free Precession Techniques in Nuclear Magnetic Resonance,” PhD thesis, Cambridge, MA: Harvard University 1952.
[34] R. V. Damadian, “Tumor detection by nuclear magnetic resonance” *Science*, vol. 171, pp. 1151–1153, March 1971.
[35] P. C. Lauterbur, “Image Formation by Induced Local Interactions: Examples of Employing Nuclear Magnetic Resonance,” *Nature*, vol. 242, pp. 190–191, 1973
[36] P. Mansfield and P. Grannell, “Diffraction and microscopy in solids and liquids by NMR,” *Physical Review*, vol. 12, no. 9, pp.3618–3634, 1975.

[37] H. C. Torrey, “Bloch Equations with Diffusion Terms.” *Physical Review*, vol. 104, no. 3, pp. 563–565, 1956.
[38] E. O. Stejskal and J. E. Tanner, “Spin Diffusion Measurements: Spin Echoes in the Presence of a Time-Dependent Field Gradient,” *Journal of Chemical Physics*, vol. 42, no. 288, 1965.
[39] D. Le Bihan and E. Breton, “Imagerie de diffusion in vivo par résonance magnétique nucléaire,” *Comptes Rendus de l'Académie des Sciences*, vol. 93, no. 5, pp. 27–34, Dec. 1985.
[40] D. Le Bihan, E. Breton, D. Lallemand, P. Grenier, E. Cabanis, and M. Laval-Jeantet, “MR Imaging of intravoxel incoherent motions: application to diffusion and perfusion in neurologic disorders,” *Radiology*, pp. 401–407, 1986.
[41] S. Warach, D. Chien, W. Li, M. Ronthal, and R. R. Edelman, “Fast magnetic resonance diffusion-weighted imaging of acute human strokes,” *Neurology*, vol. 42, pp. 1717–1723, 1992.
[42] P. van Gelderen, M. H. de Vleeschouwer, D. DesPres, J. Pekar, P. C. van Zijl, and C. T. Moonen, “Water diffusion and acute stroke,” *Magnetic Resonance in Medicine*, vol. 31, no. 2, pp. 154–163, Feb. 1994.
[43] A. G. Sorensen, F. S. Buonanno, R. G. Gonzalez, L. H. Schwamm, M. H. Lev, F. R. Huang-Hellinger, T. G. Reese, R. M. Weisskoff, T. L. Davis, N. Suwanwela, U. Can, J. A. Moreira, W. A. Copen, R. B. Look, S. P. Finklestein, B. R. Rosen, and W. J. Koroshetz, “Hyperacute stroke: evaluation with combined multisection diffusion-weighted and hemodynamically weighted echo- planar MR imaging,” *Radiology*, vol. 199, pp. 391–401, 1996.
[44] D. Le Bihan, P. Douek, M. Argyropoulou, R. Turner, N. Patronas, and M. Fulham, “Diffusion and perfusion magnetic resonance imaging in brain tumors,” *Topics in Magnetic Resonance Imaging*, vol. 5, pp. 25–31, 1993.
[45] K. Krabbe, P. Gideon, P. Wagn, U. Hansen, C. Thomsen, and F. Madsen, “MR diffusion imaging of human intracranial tumours,” *Neuroradiology*, vol. 39, pp. 483–489, 1997.
[46] P. J. Basser, J. Mattiello, and D. LeBihan, “MR diffusion tensor spectroscopy and imaging,” *Journal of Biophysics*, vol. 66, no. 1, pp. 259–267, Jan. 1986.
[47] P. J. Basser and C. Pierpaoli, “Microstructural and physiological features of tissues elucidated by quantitative-diffusion-tensor MRI,” *Journal of Magnetic Resonance*, vol. 111, no. 3, pp. 209–219, Jun. 1996.
[48] H. Hanyu, H. Shindo, D. Kakizaki, K. Abe, T. Iwamoto, and M. Takasaki, “Increased water diffusion in cerebral white matter in Alzheimer’s disease,” *Gerontology*, vol. 43, pp. 343–351, 1997.
[49] H. Hanyu, H. Sakurai, T. Iwamoto, M. Takasaki, H. Shindo, and K. Abe, “Diffusion-weighted MR imaging of the hippocampus and temporal white matter in Alzheimer’s disease,” *Journal of the Neurological Sciences*, vol. 156, pp. 195–200, 1998.
[50] D. J. Werring, C. A. Clark, G. J. Barker, A. J. Thompson, and D. H. Miller, “Diffusion tensor imaging of lesions and normal-appearing white matter in multiple sclerosis,” *Neurology*, vol. 52, no. 8, pp. 1626–1632, May 1999.
[51] M. A. Horsfield, H. B. Larsson, D. K. Jones, and A. Gass, “Diffusion magnetic resonance imaging in multiple sclerosis,” *Journal of Neurology, Neurosurgery, and Psychiatry,* vol. 64, no. 1, pp. 80–84, 1998.

[52] A. L. Tievsky, T. Ptak, and J. Farkas, "Investigation of apparent diffusion coefficient and diffusion tensor anisotropy in acute and chronic multiple sclerosis lesions," *American Journal of Neuroradiology.*, vol. 20, pp. 1491–1499, 1999.

[53] C. A. Meyers, "How chemotherapy damages the central nervous system," *Journal of Biology*, vol. 7, no. 4, 2008.

[54] S. B. Parket, D. Goldstein, A. V. Krishnan, C. S. Lin, M. L. Friedlander, J. Cassidy, M. Koltzenburg, and M. C. Kiernan, "Chemotherapy-induced peripheral neurotoxicity: a critical analysis," *CA: A Cancer Journal for Clinicians*, vol. 63, no. 6, pp. 419–437, Nov. 2013.

[55] C. Poupon, C. A. Clark, V. Frouin, I. Bloch, D. L. Bihan, and J. F. Mangin, "Tracking white matter fascicles with diffusion tensor imaging," *Proceedings of the 8th Annual Meeting ISMRM*, pp. 325, 1999.

[56] R. Xue, P.C. van Zijl, B. J. Crain, M. Solaiyappan, and S. Mori, "In vivo three-dimensional reconstruction of rat brain axonal projections by diffusion tensor imaging," *Magnetic Resonance in Medicine*, vol. 42, no. 6, pp. 1123–1127, 1999.

[57] S. Mori, B. J. Crain, V. P. Chacko, and P.C. van Zijl, "Three-dimensional tracking of axonal projections in the brain by magnetic resonance imaging," *Annals of Neurology*, vol. 45, no. 2, pp. 265–269, 1999.

[58] H. Bridge and S. Clare, "High-resolution MRI: in vivo histology?" *Philosophical Transactions of the Royal Society of London. Series B, Biological Sciences*, vol. 361, no. 1465, pp. 137–146. January 2006.

[59] M. M. Zeineh, S. Holdsworth, S. Skare, S. W. Atlas, and R. Bammer, "Ultra-High Resolution Diffusion Tensor Imaging of the Microscopic Pathways of the Medial Temporal Lobe," *Neuroimage*, vol 62, no. 3, pp. 2065–2082, Sep. 2012.

[60] S. B. Vos, M. A. Viergever, and A. Leemans, "The anisotropic bias of fractional anisotropy in anisotropically acquired DTI data." *Proceedings of the International Society for Magnetic Resonance in Medicine*, vol. 19, 2011.

[61] A. W. Anderson, "Theoretical analysis of the effects of noise on diffusion tensor imaging," *Magnetic Resonance in Medicine*, vol. 46, no. 6, pp. 1174–1188, 2001.

[62] J. Hrabe, G. Kaur, and D. N. Guilfoyle, "Principles and limitations of NMR diffusion measurements," *Journal of Medical Physics*, vol. 32, no. 1 pp. 34–42, January 2007.

[63] C. Beaulieu, "the basis of anisotropic water diffusion in the nervous system - a technical review," *NMR in biomedicine*, vol. 15, no. 7, December 2002

[64] K. D. Harkins and M. D. Does, "Simulations on the Influence of Myelin Water in Diffusion-Weighted Imaging," *Physics in Medicine and Biology*, vol. 61, no. 13, pp. 4729–4745, July 2016.

[65] G. C. Zheng, L. Tieqiang, and T. Hindmarsh, "Diffusion MRI studies of experimental animal models and patients with stroke," *Chinese Medical Journal*, vol. 112, no. 2, pp. 176–181, 1999.

[66] S. K. Song, S. W. Sun, M. J. Ramsbottom, C. Chang, J. Russell, and A. H. Cross, "Dysmyelination revealed through MRI as increased radial (but unchanged axial) diffusion of water," *Neuroimage*, vol. 17, no. 3, pp. 1429–1436, 2002.

[67] S. K. Song, S. W. Sun, W. K. Ju, S. J. Lin, A. H. Cross, and A. H. Neufeld, "Diffusion tensor imaging detects and differentiates axon and myelin degeneration in mouse optic nerve after retinal ischema," *Neuroimage*, vol. 20, no. 3, pp. 1714–1720, 2003.

[68] C. P. Lin, W. Y. Tseng, H. C. Cheng, and J. H. Chen, "Validation of diffusion tensor magnetic resonance axonal fiber imaging with registered manganese-enhanced optic tracts," *NeuroImage*, vol. 14, pp. 1035–1047, 2001.

[69] C. P. Lin, V. J. Wedeen, J. H. Chen, C. Yao, and W. Y. Tseng "Validation of diffusion spectrum magnetic resonance imaging with manganese-enhanced rat optic tracts and ex vivo phantoms," *NeuroImage*, vol. 19, pp. 482–495, 2003.

[70] Y. Gao, A. S. Choe, I. Stepniewska, X. Li, M. J. Avison, and A. W. Anderson, "Validation of DTI Tractography-Based Measures of Primary Motor Area Connectivity in the Squirrel Monkey Brain," *PLOS ONE*, vol. 8, no. 10, 2013.

[71] C. Yeh, B. Schmitt, D. Le Bihan, J. Li-Schlittgen, C. Lin, and C. Poupon, "Diffusion microscopist simulator: A general monte carlo simulation system for diffusion magnetic resonance imaging," *PLOS ONE*, vol. 8, Oct. 2013.

[72] K. H. Cho, C. H. Yeh, J. D. Tournier, Y. P. Chao, and J. H. Chen, "Evaluation of the accuracy and angular resolution of q-ball imaging," *NeuroImage*, vol. 42, pp. 262–271, 2008.

[73] J. D. Tournier, C. H. Yeh, F. Calamante, K. H. Cho, A. Connelly, and C. P. lin, "Resolving crossing fibres using constrained spherical deconvolution: validation using diffusion-weighted imaging phantom data," *NeuroImage*, vol. 42, pp. 617–625, 2008.

[74] N. Shemesh, E. Özarslan, A. Bar-Shir, P. J. Basser, and Y. Cohen, "Observation of restricted diffusion in the presence of a free diffusion compartment: Single- and double-PFG experiments," *Journal of Magnetic Resonance*, vol. 200, pp. 214–225, 2009.

[75] C. H. Yeh, K. H. Cho, H. C. Lin, J. J. Wang, and C. P. Lin, "Reduced encoding diffusion spectrum imaging implemented with a bi-Gaussian model," *IEEE Transactions on Medical Imaging*, vol. 27, pp. 1415–1424, 2008.

[76] C. H. Yeh, J. D. Tournier, K. H. Cho, C. P. Lin, F. Calamante, and A. Connely, "The effect of finite diffusion gradient pulse duration on fibre orientation estimation in diffusion MRI," *NeuroImage*, vol. 51, pp. 743–751, 2010.

[77] P. L. Hubbard, F. L. Zhou, S. J. Eichhorn, and G. J. Parker, "Biomimetic phantom for the validation of diffusion magnetic resonance imaging," *Magnetic Resonance in Medicine*, vol. 73, no. 1, pp. 299–305, 2015.

[78] M. Perrin, C. Poupon, B. Rieul, P. Leroux, A. Constantinesco, J. F. Mangin, and D. LeBihan, "Validation of q-ball imaging with a diffusion fibre-crossing phantom on a clinical scanner," *Philosophical Transactions of the Royal Society of London. Series B, Biological Sciences*, vol. 360, pp. 881–891, 2005.

[79] C. Poupon, B. Rieul, I. Kezele, M. Perrin, F. Poupon, and J. F. Mangin, "New diffusion phantoms dedicated to the study and validation of high-angular-resolution diffusion imaging (HARDI) models," *Magnetic Resonance in Medicine*, vol. 60, pp. 1276–1283, 2008.

[80] E. Fieremans, Y. De Deene, S. Delputte, M. S. Ozdemir, Y. D'Asseler, J. Vlassenbroeck, K. Deblaere, E. Achten, and I. Lemahieu, "Simulation and experimental verification of the diffusion in an anisotropic fiber phantom," *Journal of Magnetic Resonance*, vol. 190, pp. 189–199, 2008.

[81] P. Pullens, A. Roebroeck, and R. Goebel, "Ground truth hardware phantoms for validation of diffusion-weighted MRI applications," *Journal of Magnetic Resonance Imaging*, vol. 32, no. 2, pp. 482–488, August 2010.

[82] J, D. Tournier, F. Calamante, M. D. King, D. G. Gadian, and A. Connelly, "Limitations and requirements of diffusion tensor fiber tracking: An assessment using simulations," *Magnetic Resonance in Medicine*, vol. 47, no. 4, pp. 701–708, April 2002.

[83] A. Leemans, J. Sijbers, M. Verhoye, A. Van der Linden, and D. Van Dyck, "Mathematical framework for simulating diffusion tensor MR neural fiber bundles." *Magnetic Resonance in Medicine*, vol. 53, no. 4, pp. 944–953, April 2005.

[84] W. Van Hecke, J. Sijbers, S. De Backer, D. Poot, P. M. Parizel, and A. Leemans, "On the construction of a ground truth framework for evaluating voxel-based diffusion tensor MRI analysis methods," *Neuroimage*, vol. 46, no 3, July 2009.

[85] T. G. Close, J. D. Tournier, F. Calamante, L. A. Johnston, I. M. Y. Mareels, and A. Connelly, "A software tool to generate simulated white matter structures for the assessment of fibre-tracking algorithms," *NeuroImage*, vol. 47, no. 4, pp. 1288–1300, 2009.

[86] P. F. Neher, F. B. Laun, B. Stieltjes, and K. H. Maier-Hein, "Fiberfox: Facilitating the creation of realistic white matter software phantoms," *Magnetic Resonance in Medicine*, vol. 72, no. 5, pp. 1460–1470, 2013.

[87] D. Perrone, B. Jeurissen, J. Aelterman, T. Roine, J. Sijbers, A. Pizurica, A. Leemans, and W. Philips, "D-BRAIN: Anatomically Accurate Simulated Diffusion MRI Brain Data," *PLOS ONE*, vol. 11, no. 3, 2016.

[88] G. J. Stanisz, A Szafer, G. A. Wright, and R. M. Henkelman, "An analytical model of restricted diffusion in bovine optic nerve," *Magnetic Resonance in Medicine*, vol. 37, no. 1, pp.103–111, January 1997.

[89] E. Davoodi-Bojd, M. Chopp, H. Soltanian-Zadeh, S. Wang, G. Ding, and Q. Jiang, "An Analytical Model for Estimating Water Exchange Rate in White Matter Using Diffusion MRI," *PLOS*, 2014.

[90] F. Mauconduit, and H. Lahrech, "In vivo DTI parameter choice using Monte-Carlo diffusion simulations in a model of brain white matter," *Proceedings of the International Society for Magnetic Resonance in Medicine*, vol. 18, 2010.

[91] Y. Wang, and S. K. Song, "The Effect of Inflammation on DTI Derived Axial and Radial Diffusivity: A Monte Carlo Simulation Study," *Proceedings of the International Society for Magnetic Resonance in Medicine*, vol. 19, 2011.

[92] A. B. Landman, J. A. D. Farrell, S. A. Smith, D. S. Reich, P. A. Calabresi, and C. M. van Zijl, "Complex Geometric Models of Diffusion and Relaxation in Healthy and Damaged White Matter," *NMR in Biomedicine*, vol. 23, no. 2, pp. 152–162, February 2010.

[93] J. Latt, M. Nilsson, A. Rydhog, R. Wirestam, F. Stahlberg, and S. Brockstedt, "Effects of restricted diffusion in a biological phantom: a q-space diffusion MRI study of asparagus stems at a 3T clinical scanner," *Magnetic Resonance Materials in Physics, Biology and Medicine*, vol. 20, vol. 4, pp. 213–22, 2007.

[94] C. W. Chiang, Y. Wang, P. Sun, T. H. Lin, K. Trinkaus, A. H. Cross, and S. K. Song, "Quantifying white matter tract diffusion parameters in the presence of increased extra-fiber cellularity and vasogenic edema" *Neuroimage*, vol. 101, pp. 310–319, November 2014.

[95] Y. Wang and S. K. Song, "Optimizing diffusion weighting scheme by Cramer-Rao Lower Bound Analysis and Monte Carlo Simulation," *Proceedings of the International Society for Magnetic Resonance in Medicine*, vol. 20, 2012.

[96] M. G. Hall and D. C. Alexander, "Convergence and Parameter Choice for Monte-Carlo Simulations of Diffusion MRI," *Neuroimage*, vol. 61, no. 4, pp. 1000–1016, 2012.

[97] M. G. Hall and D. C. Alexander, "Quantification of increased cellularity during inflammatory demyelination," *Neuroimage*, vol. 61, no. 4, pp. 1000–1016, 2012.
[98] E. Fieremans, D. S. Novikov, J. H. Jensen, and J. A. Helpern, "Monte Carlo study of a two-compartment exchange model of diffusion," *NMR in Biomedicine*, vol. 23, no. 7, pp. 711–724, 2010.
[99] F. Liu, L. Vidarsson, J. D. Winter, H. Tran, and A. Kassner, "Sex differences in the human corpus callosum microstructure: a combined T2 myelin-water and diffusion tensor magnetic resonance imaging study," *Brain Research*, vol. 1343, pp. 37–45, July 2010.
[100] Y. Zhang, X. Zhou, J. Lu, J. Lichtman, D. Adjeroh, and S. T. C. Wong, "3D Axon Structure Extraction and Analysis in Confocal Fluorescence Microscopy Images," *Neural Computation*, vol. 20, no. 8, pp. 1899–1927, August 2008.
[101] F. Sepehrband, D. C. Alexander, K. A. Clark, N. D. Kurniawan, Z. Yang, and D. C. Reutens, "Parametric Probability Distribution Functions for Axon Diameters of Corpus Callosum," *Frontiers in Neuroanatomy*, vol .10, no. 59, May 2016.
[102] D. Liewald, R. Miller, N. Logothetis, H. J. Wagner, and A. Schüz, "Distribution of axon diameters in cortical white matter: an electron-microscopic study on three human brains and a macaque," *Biological Cybernetics*, vol. 108, no. 5, pp. 541–557, August 2014.
[103] K. A. Phillips, C. D. Stimpson, J. B. Smaers, M. A. Raghanti, B. Jacobs, A. Popratiloff, P. R. Hof, and C. C. Sherwood, "The corpus callosum in primates: processing speed of axons and the evolution of hemispheric asymmetry," *Proceedings. Biological Sciences.*, vol. 282, no. 1818, November 2015.
[104] A. V. Avram "Diffusion Tensor Imaging of Myelin Water," PhD dissertation, Duke University, GA 2011.
[105] D. Purves, G. J. Augustine, D. Fitzpatrick, et al., editors, "Increased Conduction Velocity as a Result of Myelination," *Neuroscience*, 2nd edition. Sunderland: Sinauer Associates, 2001.
[106] N. Stikov, J. S. Campbell, T. Stroh, M. Lavelée, S. Frey, J. Novek, S. Nuara, M. K. Ho, B. J. Bedell, R. F. Dougherty, I. R. Leppert, M. Boudreau, S. Narayanan, T. Duval, J. Cohen-Adad, P. A. Picard, A. Gasecka, D. Côté, and G. B. Pike, "Quantitative analysis of the myelin g-ratio from electron microscopy images of the macaque corpus callosum," *Data in Brief*, vol. 4, pp. 368–373, 2015.
[107] N. Stikov, J. S. Campbell, T. Stroh, M. Lavelée, S. Frey, J. Novek, S. Nuara, M. K. Ho, B. J. Bedell, R. F. Dougherty, I. R. Leppert, M. Boudreau, S. Narayanan, T. Duval, J. Cohen-Adad, P. A. Picard, A. Gasecka, D. Côté, and G. B. Pike. "In vivo histology of the myelin g-ratio with MRI," *Neuroimage*, vol. 118, pp. 397–405, September 2015.
[108] R. A. Hill, "Do Short-Term Changes in White Matter Structure Indicate Learning-Induced Myelin Plasticity?" *Journal of Neuroscience*, vol. 33, no. 50, pp. 19393–19395, December 2013.
[109] J. Fraher and P. Dockery, "A strong myelin thickness-axon size correlation emerges in developing nerves despite independent growth of Both Parameters," *Journal of Anatomy*, vol. 193, pp. 195–201, August 1998.
[110] C. S. von Bartheld, J. Bahney, and S. Herculano-Houzel, "The search for true numbers of neurons and glial cells in the human brain: A review of 150 years of cell counting," *Journal of Comparative Neurology*, vol. 524, no. 18, pp. 3865–3895, December 2016.

[111] Y. Bakiri, R. Káradóttir, L. Cossell, and D. Attwell, "Morphological and electrical properties of oligodendrocytes in the white matter of the corpus callosum and cerebellum," *Journal of Physiology*, vol. 589 no. 3, pp 559–573, November 2010.
[112] W. S. Price, "Pulsed-field gradient nuclear magnetic resonance as a tool for studying translational diffusion: Part 1. Basic theory," *Concepts in Magnetic Resonance*, Wiley, pp. 299–336, 1997.
[113] H. Jiang, P. C. M. van Zijl, J. Kim, G. D. Pearlson, and S. Mori, "DtiStudio: Resource program for diffusion tensor computation and fiber bundle tracking," *Computer Methods and Programs Biomedicine*, vol. 81, pp. 106–116, Jan. 2006.
[114] K. R. Hahn, R. Klaus, M. Sergej, S. Hasan, and M. Khader, "Random noise in diffusion tensor imaging, its destructive impact and some corrections," Visualization and Processing of Tensor Fields. Mathematics and Visualization. Berlin: Springer, Heidelberg, 2006.
[115] H. Gudbjartsson and S. Patz, "The Rician Distribution of Noisy MRI Data," *Magnetic resonance in medicine*, vol. 34, no, 6, pp. 910–914, 1995.
[116] M. S. van der Knaap and J. Valk, "Magnetic Resonance of Myelination and Myelin Disorders," New York: Springer, 2005.
[117] T. Kuhlmann, G. Lingfield, A. Bitsch, J. Schuchardt, and W. Bruck, "Acute axonal damage in multiple sclerosis is most extensive in early disease stages and decreases over time," *Brain*, vol. 125, pp. 2202–2212, 2002.
[118] A. Compston and A. Coles, "Multiple sclerosis," *Lancet*, vol. 372, no. 9648, pp.1502–1517, October 2008.
[119] I. D. Croall, J. A. C. Cowie, and H. Jiabao, "White matter correlates of cognitive dysfunction after mild traumatic brain injury," *American Academy of Neurology*, 2014.
[120] D. Reyes-Haro, E. Mora-Loyola, B. Soria-Ortiz and J. García-Colunga, "Regional density of glial cells in the rat corpus callosum," *Biological Research*, vol. 46, no. 1, 2013.
[121] M. N. Edelmann, K. R. Krull, W. Liu, J. O. Glass, Q. Ji, R. Ogg N. D. Sabin, D. K. Srivastava, L. L. Robison, M. M. Hudson, and W. E. Reddick, "Diffusion tensor imaging and neurocognition in survivors of childhood acute lymphoblastic leukaemia," *Brain*, vol. 137, no. 11, November 2014.
[122] S. Berman, K. L. West, M. D. Does, J. D. Yeatman, and A. A. Mezer, "Evaluating g-ratio weighted changes in the corpus callosum as a function of age and sex," *Neuroimage*, vol. 1, no. 10, 2017.
[123] M. Laganà, M. Rovaris, A. Ceccarelli, C. Venturelli, S. Marini, and G. Baselli, "DTI Parameter Optimisation for Acquisition at 1.5T: SNR Analysis and Clinical Application," *Computational Intelligence and Neuroscience*, vol. 2010, 2010.
[124] G. Andreise, L. M. White, A. Kassner, G. Tomlinson, and M. S. Sussman, "Diffusion tensor imaging and fiber tractography of the median nerve at 1.5T: optimization of b value," *Skeletal Radiology*, vol. 38, no. 1, pp. 51–59, January 2009.
[125] T. W. Redpath, "Signal-to-noise ratio in MRI," *The British Journal of Radiology*, vol. 71, pp. 704–707, 1998.
[126] H. Peng and K. Arfanakis, "Diffusion Tensor Encoding Schemes Optimized for White Matter Fibers with Selected Orientations," *Proceedings of the International Society for Magnetic Resonance in Medicine*, vol.14, 2006.
[127] X. Yao, Y. Lu, T. Yu, Q. Huang, Y. Wang, and S. Zhuang, "Optimization of Number of Diffusion Gradient Directions on anisotropy indices and deterministic fiber tracking for

diffusion tensor imaging," *Proceedings. International Conference on Natural Computation*, 2013.
[128] D. C. Alexander and G. J. Barker, "Optimal imaging parameters for fiber-orientation estimation in diffusion MRI," *NeuroImage*, vol. 27, no. 2, pp. 357–367, 2005.
[129] O. Brihuega-Moreno, F. P. Heese, and L. D. Hall, "Optimization of diffusion measurements using Cramer-Rao lower bound theory and its application to articular cartilage," *Magnetic Resonance in Medicine*, vol. 50, no. 5, pp. 1069–76, November 2003.
[130] W. Gao, H. Zhu and W. Lin, "A Unified Optimization Approach for Diffusion Tensor Imaging Technique," *NeuroImage*, vol. 44, no. 3, pp. 729–741, 2009.
[131] P. B. Kingsley and W. G. Monahan, "Selection of the optimum b factor for diffusion-weighted magnetic resonance imaging assessment of ischemic stroke," *Magnetic Resonance in Medicine*, vol. 51, no. 5, pp. 996–1001, May 2004.
[132] I. E. Evangelou, A. Serag, M. Bouyssi-Kobar, A. J. du Plessis and C. Limperopoulos, "Optimized Methodology for Neonatal Diffusion Tensor Imaging Processing and Study-specific Template Construction," *Proceedings of the International Conference of the IEEE Engineering in Medicine and Biology Society*, 2014.
[133] C. E. Shannon, "A Mathematical Theory of Communication", *Bell System Technical Journal*, vol. 27, no. 3, pp. 379–423, July 1948.
[134] E. Y. Kim, H. J. Park, D. H. Kim, S. K. Lee, and J. Kim, "Measuring Fractional Anisotropy of the Corpus Callosum Using Diffusion Tensor Imaging: Mid-Sagittal versus Axial Imaging Planes," *Korean Journal of Radiology*, vol. 9, no. 5, pp. 391–395, 2008.
[135] E. Mormina, M. Longo, A. Arrigo, C. Alafaci, F. Tomasello, A. Calamuneri, S. Marino, M. Gaeta, S. L. Vinci, and F. Granata, "MRI Tractography of Corticospinal Tract and Arcuate Fasciculus in High-Grade Gliomas Performed by Constrained Spherical Deconvolution: Qualitative and Quantitative Analysis," *AJNR American Journal of Neuroradiology*, vol. 36, no. 10, pp. 1853–1858, October 2015.
[136] D. C. Dean, J. O'Muircheartaigh, H. Dirks, B. G. Travers, N. Adluru, A. L. Alexander, and S. C. L. Deonidgh, "Mapping an index of the myelin g-ratio in infants using magnetic resonance imaging," *NeuroImage*, vol. 132, pp. 225–237, May 2016.
[137] D. Liewald, R. Miller, N. Logothetis, H. J. Wagner, and A. Schüz, "Distribution of axon diameters in cortical white matter: an electron-microscopic study on three human brains and a macaque". *Biological Cybernetics*, vol. 108 , no. 5, pp. 541–557, 2014.
[138] Anat Anz, "Diameter of axons and thickness of myelin sheaths of the pyramidal tract fibres in the adult human medullary pyramid," *Graf von Keyserlingk D, Schramm U.*, vol. 157, no. 2, pp. 97–111, 1984.
[139] S. Mohammadi, D. Carey, F. Dick, J. Diedrichsen, M. I. Sereno, M Reisert, and N. Weiskopf, "Whole-Brain *In-vivo* Measurements of the Axonal G-Ratio in a Group of 37 Healthy Volunteers," *Frontiers in Neuroscience*, vol. 9, 2015.
[140] D. S. Tuch, "High angular resolution diffusion imaging reveals intravoxel white matter fiber heterogeneity," *Magnetic Resonance in Medicine*, vol. 48, no. 4, pp. 577–582, 2002.
[141] D. S. Tuch, "Q-ball imaging," *Magn. Reson. Med.*, vol. 52, pp.1358–1372, 2004.
[142] P. T. Callaghan, "Principles of nuclear magnetic resonance microscopy," Oxford: Oxford University Press, 1991.

[143] Y. Assaf, R. Z. Freidlin, G. K. Rohde, and P. J. Basser, "New modeling and experimental framework to characterize hindered and restricted water diffusion in brain white matter," *Magnetic Resonance in Medicine*, vol. 52, pp. 965–978, 2004.
[144] J. D. Tournier, F. Calamante, D. G. Gadian, and A. Connely, "Direct estimation of the fiber orientation density function from diffusion-weighted MRI data using spherical deconvolution." *NeuroImage*, vol. 23, no. 3, pp. 1176–1185, 2004.
[145] E. J. Canales-Rodríguez, L. Melie-García, and Y. Iturria-Medina. "Mathematical Description of q-Space in Spherical Coordinates: Exact q-Ball Imaging," *Magnetic Resonance in Medicine*, vol. 61, no. 3, pp. 1350–1367, 2009.
[146] C. P. Hess, P. Mukherjee, E. T. Han, D. Xu, and D. B. Vigneron, "Q-Ball Reconstruction of Multimodal Fiber Orientations Using The Spherical Harmonic Basis," *Magnetic Resonance in Medicine*, vol. 56, p.104–117, 2006.
[147] F. Dell'acqua, P. Scifo, G. Rizzo, M. Catani, A. Simmons, G. Scotti, and Fazio F. "A modified damped Richardson-Lucy algorithm to reduce isotropic background effects in spherical deconvolution," *Neuroimage*, vol. 49, no. 2, pp. 1446–1458, 2010.